MICROMACHINED NANOPOROUS MEMBRANES FOR BLOOD OXYGENATION SYSTEMS

by

VIJAYAKRISHNAN AMBRAVANESWARAN

Presented to the Faculty of the Graduate School of

The University of Texas at Arlington in Partial Fulfillment

of the Requirements

for the Degree of

MASTER OF SCIENCE IN ELECTRICAL ENGINEERING

THE UNIVERSITY OF TEXAS AT ARLINGTON

August 2008

ACKNOWLEDGEMENTS

As the saying goes 'Life is a journey' and I feel that a journey becomes easier when we travel together. This thesis is the end of my long journey in obtaining my degree in Electrical Engineering and I did not travel this journey in vacuum. I have been accompanied by many people and it is satisfying that I have an opportunity to thank them.

First a very special thanks to my advisor Prof. Zeynep Celik-Butler.

Prof. Celik-Butler gave me the confidence and support to begin my master's thesis in Electrical Engineering. With her enthusiasm, her inspiration, and her great efforts to explain things clearly and simply, she helped to make this journey fun for me. Throughout my master's degree, she provided encouragement, sound advice, preeminent teaching, enjoyable company, and many good ideas. I would have been lost without her. Thank you Prof. Celik-Butler.

I would also like to thank my committee members Prof. Richard Billo, Prof. Jung-Chih Chiao, Prof. Robert Eberhart, and Prof. Samir Iqbal for taking time from their schedules to review my thesis helping me in pursuit of my master's degree. I am also thankful to Prof. Robert Eberhart and Prof. Cheng-Jen Chuong of UTA Bioengineering department for their suggestions and advise throughout my master's thesis. Their experience and knowledge were enlightening. I would also like to thank Prof. Richard Billo of Dean of Engineering and Dr. Michael A. Savitt of Midwest Heart Surgery Institute for their support and suggestions.

I would like to extend my gratitude towards Dr. Nasir Basit, manager, NanoFAB center, Dr. Fatima Amir and Mr. Dennis Bueno, Research Engineering Scientist NanoFAB center for helping me throughout my work in clean room. I would also like to express my appreciation to Paul Logan, Equipment Technician, NanoFAB center. I would like to acknowledge the help of my co-workers Suraj, Siva, Murali, Shariar, Tanvir, Mukti Rana, Aamer, Srikumar Erikn and all my colleagues for their company and friendship throughout my journey. I am very thankful to all my friends who helped my during my masters work indirectly.

I would like to express my indebtedness to all my family members and friends.

This work was supported by Midwest Heart Surgery Institute, 2901 W. Kinnickinnic River Parkway Suite 511 Milwaukee, WI 53215 USA.

July 14, 2008

ABSTRACT

MICROMACHINED NANOPOROUS MEMBRANES FOR BLOOD OXYGENATION SYSTEMS

VIJAYAKRISHNAN AMBRAVANESWARAN, M.S.

The University of Texas at Arlington, 2008

Supervising Professor: Zeynep Celik-Butler

An oxygenator is a medical device that aids in the exchange of oxygen and carbon dioxide in the human blood during procedures and illnesses that may cause the interruption or cessation of blood flow in the body. Porous membranes currently used in blood-oxygenation systems are bulky, and the pores are relatively large in dimension. The control over the pore size is poor due to the fabrication techniques used. The standard deviation of the pore size and the placement of the pores deteriorate even further with decreasing pore diameter. It is because of inaccurate pore placement and poor control over the porosity the oxygenation of blood in current oxygenation systems is low. Control of the feature size and consistent topography of the nanopores will make long-term pulmonary blood oxygenation possible, which was not within reach previously. Fabrication of nanoscale features with precise placement and control have been realized with advancements in Microelectromechanical Systems (MEMS) fabrication techniques. This led to the development of micromachined nanoporous membranes for blood-oxygenators, which is the focus of this work. The blood oxygenator designs were modeled, simulated, and optimized to increase

the gas exchange efficiency. In order to achieve increased blood gas exchange rate, a balance between the blood and gas volume should be achieved, and the surface area of gas exchange should be increased. The blood oxygenator designs were modeled to preserve microscale blood channel dimensions, thereby permitting the red cell shape change that enhances gas exchange in the pulmonary capillary. The membrane material was experimentally identified as low-pressure chemical vapor deposited (LPCVD) silicon nitride owing to its high stability, ease of deposition and resistance to etchants. Potassium hydroxide was chosen as the etchant for silicon because of its elevated etch selectivity in the (100) plane of silicon and high etch rate to form the channels for the flow of gas. Different techniques like Focused Ion Beam (FIB) and nanoimprinting were used to fabricate pores on the membrane. The membranes were simulated for displacement followed by stress / strain analysis. The porous membranes were experimentally examined for stability under pressure and the results were verified using finite element modeling (FEM). The experimental results and the FEM analysis showed good agreement under normal operating conditions. Due to intrinsic problems in FIB like sequential drilling of the pores and inaccurate stage control, another technique, nanoimprinting, was eventually adopted for pore patterning and etching. Upon analysis, the imprinting indicated good transfer of pattern from the mold to the resist. The pore dimensions ranged from 180 nm - 220 nm. Subsequently, nanoporous membranes were fabricated and the membranes were releases by bulk micromaching of silicon. Future work involves development of blood channels and manifolds for input and output of blood and gas channels.

TABLE OF CONTENTS

LIST OF FIGURES

LIST OF TABLES

CHAPTER 1

INTRODUCTION

When we hear the word Microelectromechanical system or MEMS, the first picture, which comes to our mind, is a tiny network moving parts, which has replaced a macro moving parts. For long MEMS have been tagged to moving parts and mechanical structures. More recently, the improvement in fabrication techniques has helped in producing structures, which are of sub-micron scale. These improvements have contributed to the emergence of a new field, nanobioscience, which has started to revolutionize the way patients are to be treated. Two expanding areas of this field are patient monitoring and the delivery of drugs. The devices required for such operation are sometimes required to operate inside or on the human body.

To fabricate devices that can operate in-vivo, the size of the device has to be in sub-millimeter scale, and should have minimal adverse impact on the human body. MEMS fabrication techniques for long have been used to fabrication of devices at such scales. Devices required to operate in in-vivo conditions can be aseptically fabricated, and sealed in vacuum using MEMS technology. The other major advantage, which MEMS technology offers, is repeatability and uniformity compared to other technologies used for producing these devices. These features maybe usefully employed in improving the performance of blood oxygenators, and area that has seen little advance in the last two decades.

1.1 Purpose of research

It is estimated that about 18-20 million people suffer from chronic lung disease. [1] Patients with lung disease can prolong their survival with a lung transplant. However, with limited donors, lung implants are difficult. The number of people diagnosed with heart and lung disease increase every day. In US alone, there are around 1200 lung transplants every year. The chance of survival without a transplant for such patients is low. [2]

The other option for patients with chronic lung disease is an artificial lung implant, which can help in oxygenation of blood. Currently used blood oxygenation devices are relatively bulky in size and are not of implantable scale. They are mainly used for temporary, external oxygenation of blood. At present, blood oxygenation systems have membranes made from polymer, whose pore dimensions, and porosities are not controlled. This allows the pores to become into hydrophilic passages, in turn allowing water and plasma to flow from the blood side to the gas side. Thus, the membrane needs to be replaced every six hours, which limits the possibility of an implantable lung.

1.1.1 Goals

The goal of this M.S. thesis is to fabricate a robust porous membrane, which overcomes the defects in the currently used porous membranes in blood oxygenation systems. Ideally, the pores on the membrane have to be of uniform size, straight through the membrane, and the membrane must be of precisely controlled porosity. Moreover, the pore distribution has to be uniform on the membrane. The membrane should be biocompatible, and should not initiate host defense mechanism, or damage blood cells.

1.2 Accomplishments

- Designed and evaluated the performance of four different blood oxygenator designs and down selected two designs for fabrication.
- Experimentally identified materials for fabrication of robust membranes.
- Fabricated low porosity membranes using FIB and tested for mechanical stability.
- Developed a process for fabrication of pores using nanoimprinting and demonstraed pilot results to show potential for reaching the goals.

1.3 Organization of thesis

Chapter 1 gives a detailed discussion on the review of micromachining and about the different types of blood oxygenation systems. In addition, the currently used membrane lung is compared to the natural lung. The Chapter concludes with a section on how microfabrication can improve blood oxygenation. Chapter 2 discusses the details of different silicon channel membrane oxygenator designs. The Chapter also gives the process flows for different designs and comparison of different designs, identifying two optimized models. Chapter 3 titled *Focused Ion Beam* gives a detailed account on the working of a FIB system. The Chapter also discusses in detail, the process flows for fabrication of test membranes. Chapter 4 titled *Nanoimprinting* discusses about different types of nanoimprinting processes. The second part of the Chapter details the process flow for fabrication of pores using the nanoimprinter. Chapter 5 summarizes the results and concludes the thesis with recommendations for future experiments and analysis towards the development of an artificial lung.

1.4 Review of blood oxygenation

Respiration is a very important process that takes place in all living things, at all times. It is a release of energy from glucose or other organic substances inside living cells. Every cell requires to respire in order to produce the energy it needs and to survive. There are two types of breathing (respiration) i.e. External and Internal.

- *External*: External respiration occurs with the exchange of oxygen and carbon dioxide between the environment and the organism.
- *Internal*: Internal respiration occurs when the oxygen and carbon dioxide from the atmosphere are transferred to the tissues and the capillary where they are being stored.

The basic flow of oxygen from the atmosphere to the tissue is as follows:

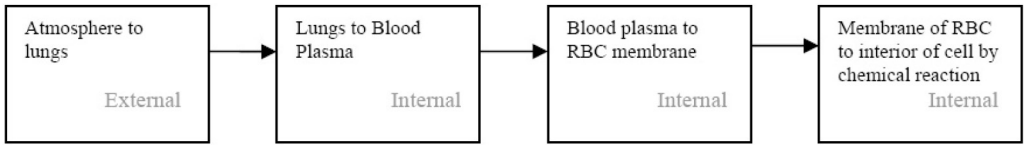

Figure 1.1. Flow of oxygen from atmosphere to tissue.

As the oxygen flows from the nasal passage to the alveoli - capillary membrane, and to the RBC (red blood cell) it undergoes a repeat process of airway bifurcation, of twenty three times. The first sixteen bifurcations encompass the conductive zone where the oxygen is pumped in and out of the lungs. The remaining seven bifurcations form the transitional, and the respiratory zones, circulating in the alveolus, where the gas exchange occurs between the capillary blood, and the air. This is one of the primary reasons behind the increase in surface area of the gas exchange; this is about 2000 times the circumference of the trachea

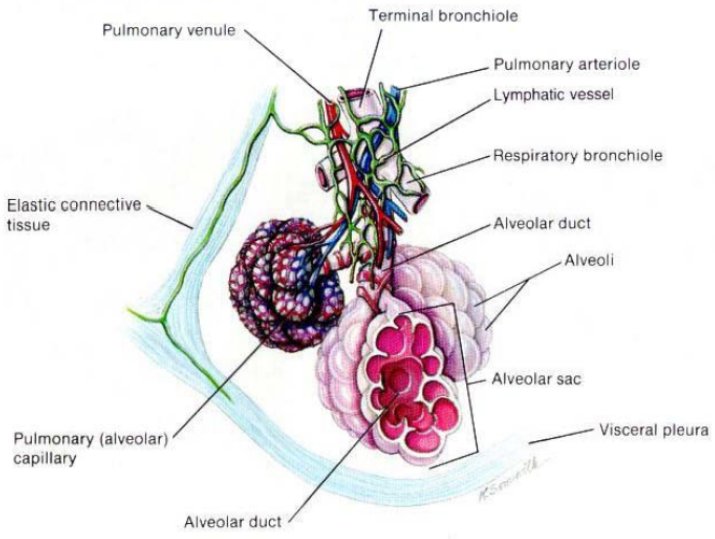

Figure 1.2. Gas flow from trachea to avelora sacs [3].

In certain abnormal conditions, this transference of the gas from the external atmosphere into the human body can be hampered to an extent that it calls for a replacement or alternatively requires an external support system that monitors and manages the lung to function normally. The external support system for this proper transference of gas between the lungs and the blood is known as a blood oxygenator. An oxygenator is a unit whose sole function is to oxygenate the blood and remove the carbon dioxide content in the blood.

There are two types of oxygenator, they are

- Bubble oxygenator
- Membrane oxygenator

1.4.1 Bubble oxygenator

The blood from the veins enters the mixing chamber where it encounters the gas (oxygen) for the first time. The gas from the pump is pumped into the chamber

and sufficient time is allowed for the recombination of the gas and the blood. Once the blood is diffused with the gas, it follows a time gap that allows the diffused blood to remain there idle for a stipulated time. Thereafter it is allowed to flow to the heat exchanger, into the reservoir. Figure 1.3 shows the cross-section of a bubble oxygenator.

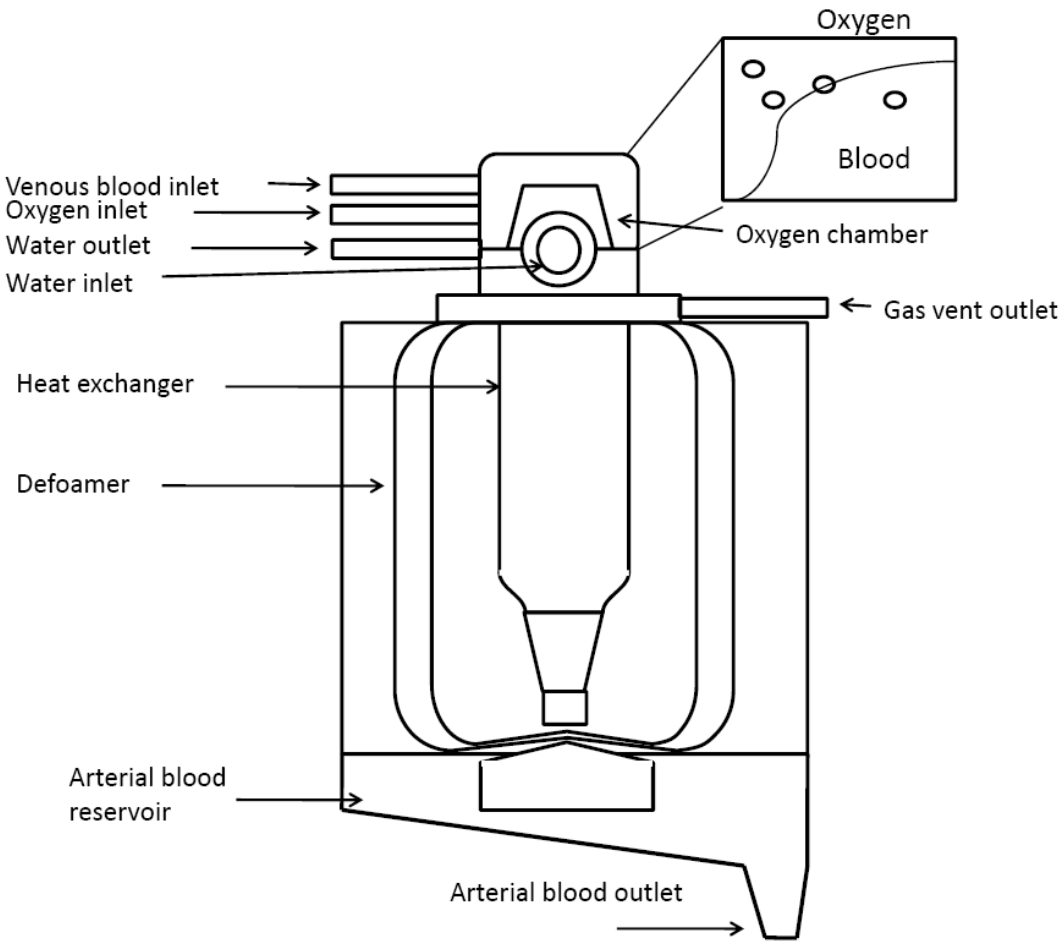

Figure 1.3. Cross-section of a typically used bubble oxygenator.

The diffused gas bubbles are then separated in two ways:

- They are first allowed to flow through a filter of perforation (much smaller than the size of the bubble) that permit only the blood to pass through and not the bubbles.
- The other way of elimination of the gas bubble is by absorption of the bubbles into the red blood cells where it reacts with the cell to reach the tissue. The absorption of oxygen by the tissue depends upon the partial pressure of the oxygen of the blood which can be calculated as follows [4]:

$$P_b + ST - \sum PP \tag{1.1}$$

where,

- P_b is the ambient pressure of blood,
- ST is the surface tension of blood, and
- PP is the partial pressure of CO_2 and O_2

The absorption of gas into blood is improved, by increasing the partial pressure of the oxygen. This is achieved by decreasing the size of bubbles which are to be diffused with the blood (i.e.), the size of the nozzle which is employed to diffuse the gas into the blood is reduced keeping the gas flow constant. This decrease in the size of the bubbles helps increase the partial pressure of the gas, which in turn enhances the gas and blood interaction. Although, decreasing the size of the bubbles implies an increase in the partial pressure of the carbon dioxide, the transfer of carbon dioxide from the blood side to the gas side is affected. Thus, a trade off is maintained between the bubble size and the surface area so that the transfer of CO_2 is made as easy as possible [4].

Operation of the bubble oxygenator is quite simple and is as explained above. Blood enters the mixing chamber, and the oxygen is pumped inside the chamber. The number of bubbles, which are to be diffused, is increased by making a large number

of perforations at the nozzle of the pump. This helps in increasing the surface area of the bubble to gas interaction, which assists in the absorption of the gas. One of the alternative ideas, which were used for this, was to use an inert gas along with the oxygen but the problem in using an inert gas with oxygen is that the absorption rate of inert gas is lower than oxygen, and it also hampers the absorption of oxygen by the blood. Another important criterion is to maintain adequate volume of blood in the chamber, to ensure proper absorption of gas. Maintaining a high volume of blood in the chamber also reduces the chance of bubble escaping to the top, thus reducing the usage of defoaming agents. The high volume of blood in the reservoir also enables us to maintain the rate at which the blood is pumped [4].

Primary advantages:

- The Bubble oxygenator has a low blood pressure drop, which is of the order of 30 cm of water compared to a pressure of 100 cm of water in membrane oxygenators.
- The major advantage of bubble oxygenator is that it can be placed upstream of the blood pump, since it has low pressure drop.
- Another advantage of using bubble oxygenator is that there is no need for a separate reservoir for artery as the oxygenation unit has an inbuilt reservoir.

The primary reason bubble oxygenators are not used frequently in current practice is because of the relatively high red blood cell damage rate (hemolysis) in comparison to the membrane oxygenator.

1.4.2 Membrane oxygenator

The other type of widely used oxygenator is the membrane oxygenator. This is an oxygenator, which is analogous to natural lungs. There are two types of membrane oxygenator: true membrane and microporous membrane. True membrane oxygenator

is one, which is very similar to lungs. It has a membrane, which is used to separate the blood flow from the gas flow. The interaction of the gas and the blood purely depends upon the diffusion capacity of the gas in the membrane. The gas has to diffuse through the membrane to diffuse into the blood and then oxygenate the blood; this increases gas exchange resistance. True membrane oxygenator is relatively expensive to manufacture. Therefore, the commonly used membrane oxygenator is the microporous membrane oxygenator. Figure 1.4 depicts the schematics of typically used microporous polypropylene hollow fiber membrane oxygenator.

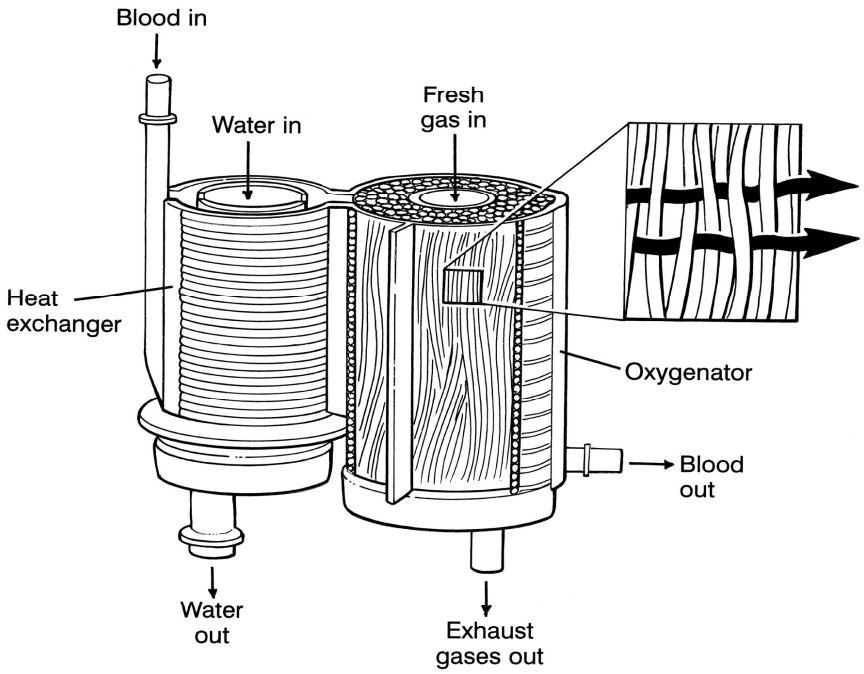

Figure 1.4. Schematics of a microporous polypropylene hollow fiber membrane blood-oxygenator [5].

Microporous membrane oxygenators are available in various surface areas, from $0.5m^2$ to $4.5m^2$ and hence can be used over a wide range of patients (from children to adults). Initially, in these membrane oxygenators, the blood and gas are separated by the hydrophobic polypropylene membrane even though pores are present. The surface tension in the pores is high owing to the hydrophobic nature of the polymer. After a certain period of operation, due to the constant interaction of the membrane with blood, a layer of protein is deposited on the membrane pores. Once the membrane is partially coated with the protein, the transfer of gas, from gas side to blood side is reduced. Initially, the blood will not permeate to the other side of the membrane, because of the higher surface tension but the protein layer reduces the surface tension allowing plasma to penetrate the pores [4]. The membrane capacity thus decreases over a period, and consequently the gas exchange decreases.

There are two types of microporous membrane oxygenators: hollow fiber and folded sheet envelope type [6]. The pore size in both types is typically about 1 μm. There are two types of the hollow microporous membrane oxygenators, classified by the blood flow, as inside and outside. The inside type is not considered efficient since the blood pressure drop is too high. In the outside blood flow type, there are two different types depending upon the direction of blood flow. The flow of blood in the outside type can be either opposite direction to the flow of gas (counter flow), or it can be in same direction (i.e.) parallel to the flow of gas. The counter flow design is more efficient.

1.4.3 Comparison of membrane lung to natural lung

In Table 1.1, a comparison of natural lung to currently used membrane lung is made. The first column gives the various figures of merit, while the second and the third columns give the value of the corresponding parameters for the membrane and

Table 1.1. Comparison of natural lung to membrane lung

Characteristics	Membrane Lung[7]	Natural Lung [8]
Surface area (m^2)	0.5-4	70
Blood path width (μm)	200	8
Blood path length (μm)	250,000	200
Membrane thickness (μm)	150	0.5
Maximum oxygen transfer (ml/min.) STP	400-600	2000

the natural lung, respectively. The first parameter considered is the surface area of interaction of the blood path with the gas path. This is the area where the blood and gas interacts with each other and gas exchange takes place. In natural lung, the surface area of interaction is 70 m^2 which is almost 18 times the maximum capacity of the membrane lung. The second parameter, which is considered, is the blood path width. The blood path width is the total width of the blood flow channel. In natural lung the value of blood path width is 8 μm. Such a small width in the blood flow channel ensures that the RBC changes its shape from a sphere to a parachute, which ensures good gas exchange. The other advantage is that since the blood path width is narrow, the RBC touches the membrane thus increasing the possibility of being oxygenated. In membrane lung, the blood path width is 200 μm. This value is excessively high and causes very high resistance for the oxygenation of RBC.

When we consider the length of the blood channel, the membrane oxygenator has a blood channel length of up to 25 cm or 250000 μm. This is to ensure that the blood cells are oxygenated completely, as the width of blood path is comparatively large. In the natural lung, the length of blood channel is about 200 μm, which is like

one thousandth of the length of the membrane lung. The thickness of the membrane is of the order of 0.5 μm in natural lung. This greatly reduces the resistance on gas transfer. The thickness of the membrane used in membrane lung is of the order of 150 μm. This makes it difficult for the gas to permeate through the thick membrane, thus reducing the efficiency. The oxygen transfer rate of the natural lung is 5 times greater than that of the membrane lung. This is one of the major shortcomings of the membrane lung.

1.4.4 How microfabrication can improve blood oxygenation.

The comparison of the membrane lung to natural lung made in the earlier section clearly indicates several shortcomings of the currently used membrane lung. These limitations can be overcome using the microfabrication techniques. With the help of microfabrication techniques, we can mimic the working of the natural lung by creating similar channel dimensions. For instance, a blood path width of 8 μm, similar to that of a pulmonary capillary can be achieved using surface micromachining. The thickness of the membrane can be reduced to approximately the membrane thickness of the natural lung by thin film deposition. The combination of blood channels approaching capillary dimensions, and ultra thin bounding porous membranes is expected to increase the oxygen transfer rate. A theoretical analysis that illustrates this feature has been published [9]. An accompanying editorial added weight to the analysis. Basically, the red blood cell in the channels of this size converts from the torpedo shape to parachute shape. The skirts of the parachute sweep the membrane surface, reducing the diffusion gap; significantly increasing oxygen transfer efficiency. The surface area of interaction of for the blood and gas channels can be maximized by surface and bulk micro-machining processes. Thus, by fabricating an environment close to the natural lung we can expect the blood oxygenation to improve consider-

ably. Figure 1.5 gives the electrical analogy of the gas exchange mechanism. The left side of the figure shows the blood channel resistance as R_b, the membrane resistance as R_m and the gas resistance as R_g. The high voltage applied on the electrical side is that of the pressure difference in the gases in the oxygenator side. When we compare the currently used membrane lung to the microfabricated blood oxygenator, we have, the blood resistance R_b is common to both oxygenators, and gas resistance R_g is negligible in both cases. The important resistance which comes into picture is the resistance of the membrane R_m. The thickness of the currently used membrane is approximately 150 μm which increases the resistance of the membrane to the gas diffusion. In the case of the microfabricated blood oxygenator the membrane can be fabricated in the order of 1-2 μm which decreases the resistance, thus allowing the current to flow freely (i.e.) reducing the gas exchange resistance by increasing the gas permeation through the membrane.

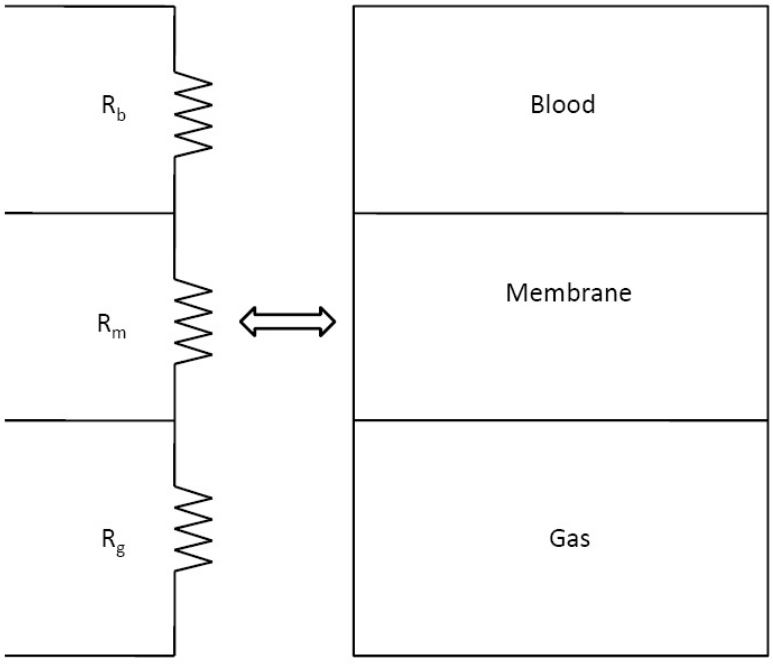

Figure 1.5. Electrical analogy to membrane gas exchange.

1.5 Review of silicon micromachining

Micromachining or etching is known as the process of removal of material at selected regions. The substrate can be removed in two ways, wet and dry etching. In wet etching, chemicals are used to react with the substrate to form soluble products, which is dissolved in the chemicals and removed. In dry etching, plasma is used for etching the substrate. Heavy atoms are allowed to bombard on silicon surface, which remove the silicon form the surface. The etching in this case can be with physical or chemical.

Other important terms in etching of silicon are isotropic, anisotropic etching, aspect ratio, surface and bulk micromachining. In *isotropic etching*, the substrate is removed equally in all directions from the exposed region. *Anisotropic* etching is just the opposite of isotropic etching, where the etching direction can be controlled. The etching direction in silicon cam be selected to achieve a particular shape in anisotropic etching.

Aspect ratio in etching is defined as the ratio if depth of etching to the width of etching in a particular etch process.

Surface micromachining can be described as the process of removing layers on top of the substrate without etching much of the substrate (silicon). It uses the substrate as a base for fabrication of devices. In surface micromachining, the substrate is not affected and the etching depth generally varies from few microns to a maximum of ten microns on top of the substrate. Surface micromachining can be either a dry or a wet etching process. Generally, surface micromachining is done to remove the sacrificial layer to release the structure.

Bulk micromachining is defined as the process of removing much of the substrate to make the structures. In this process, we form large pits, which forms the devices along with the layers deposited on the substrate. In bulk micromachining, the depth of

etching varies from few tens of microns to hundreds of microns. Bulk micromachining is generally done using wet etching mechanisms.

1.5.1 Isotropic etching of silicon

Isotropic etching of silicon can be done using both wet and dry etching mechanisms. The common isotropic wet etchant for silicon is HNA which is a mixture of hydrofluoric acid (HF), nitric acid (HNO_3) and acetic acid (CH_3COOH).The nitric acid in the solution acts as the oxidizing agent. It oxidizes the silicon and removes the silicon form the surface of the substrate. The fluorine ions from the hydrofluoric acid react with oxidized silicon to from a soluble compound in the solution. The acetic acid in the solution is used to prevent the dissociation of the nitric acid into other compounds, which helps in the formation of the oxidizing compounds.

The general reaction can be summarized as follows:

1. Acid attacks the silicon in the surface to form Si ions,
2. Reaction with the OH group to form the $Si(OH)_2^{2+}$
3. The compound of silicon with the OH group reacts with the complexing agent in the solution
4. Dissolution of the resulting compound in the solution

The general equation for the reaction is given below

$$2e^- + HNO_2 + HNO_3 + H_2O \rightarrow 2HNO_2 + 2OH^- \tag{1.2}$$

This equation clearly shows that the etching reaction is a charge driven process. Therefore, if we have any external charge we can considerably change the etch rate of the solution [10].

1.5.2 Anisotropic etching in silicon

Anisotropic etching or orientation dependent etching can be achieved in certain wet etchants and in certain dry etching processes. Silicon, which has the crystal structure as that of diamond, has different planes in its structure. Some wet etchants as alkali hydroxides show preferential etching to some of the planes when compared to others. The preferential etching in silicon is attributed to anisotropy in etching. The anisotropy in etching is taken to advantage in making MEMS devices. The structures, which we obtain, will depend on the dominant plane of the wafer. For instance when we etch a (100) dominant plane wafer in potassium hydroxide we get a 'V groove ' in the wafer depending on the size of the opening. Figure 1.6 (a) depicts th etching of a (100) dominant plane in KOH. When we use a (110) dominant plane wafer in potassium hydroxide we will get a square pit instead of a 'V grove' as in the case of (100). Figure 1.6 (b) shows the etching of a (110) dominant plane in KOH. Potassium hydroxide etches the (110) plane faster than the (100) plane and the (100) plane much faster than (111) plane.

1.5.3 Anisotropic etchants

Some of the commonly used anisotropic etchants are potassium hydroxide (KOH), ammonium hydroxide (NH_4OH), tetramethyl ammonium hydroxide (TMAH), ethylene diamine pyrochatechol (EDP), hydrazine, amine gallates. KOH is the most commonly used anisotropic wet etchant for etching silicon. Seidel in 1987 first demonstrated the anisotropy in etching of silicon by KOH [10].

The theory behind the etching of silicon in any alkali hydroxide can be given as follows:

$$Silicon + Hydroxides + Water \rightarrow Silicates + Hydrogen \tag{1.3}$$

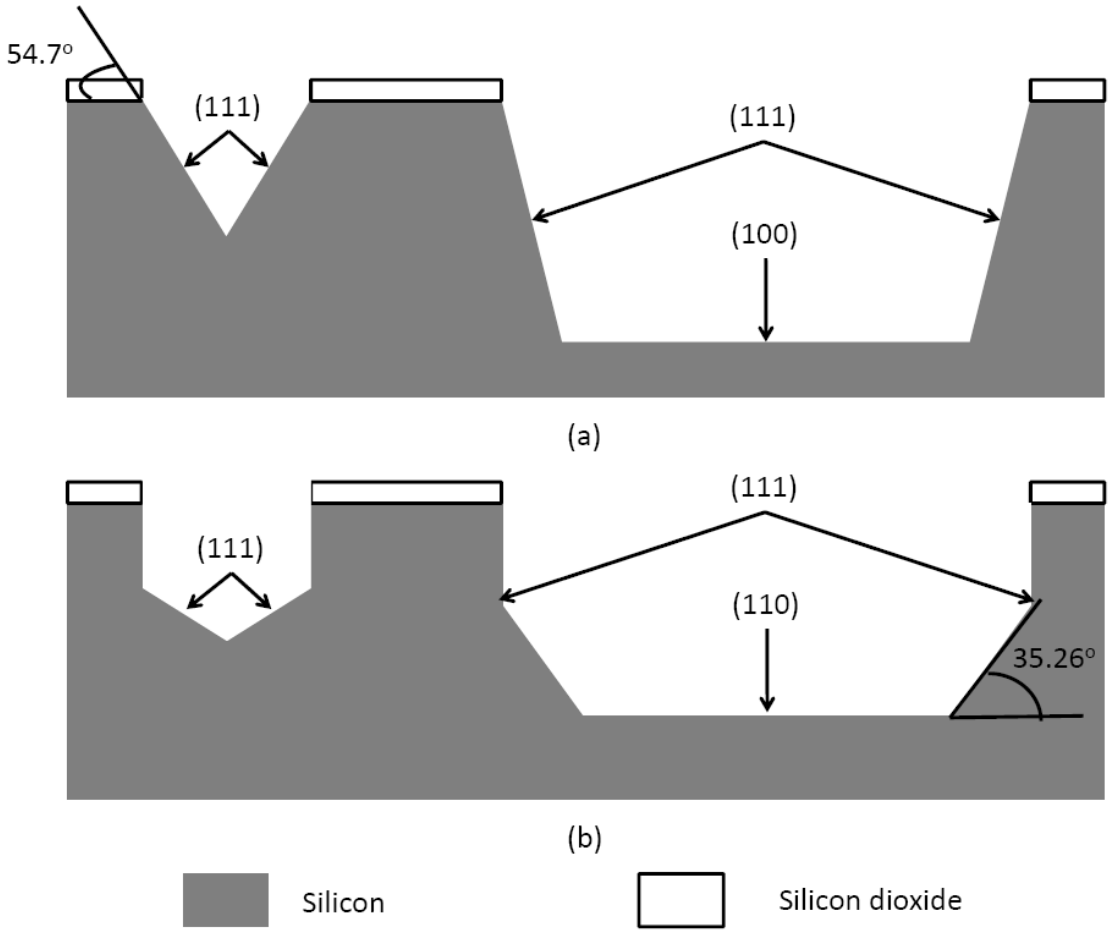

Figure 1.6. (a)Cross-section of (100) plane wafer; (b)Cross-section of (110) plane wafer.

The silicon on the surface of the substrate reacts with the hydroxides to form the hydrated silica with the release of electrons from the conduction band of silicon, which is described below:

$$Si + 2OH^- \rightarrow Si(OH)_2^{2+} + 4e^- \tag{1.4}$$

The four electrons released in this reaction reduce the water to hydroxide ions with the release of hydrogen, which is given as follows:

$$4e^- + 4H_2O \rightarrow 4OH^- + 2H_2 \tag{1.5}$$

The hydrated silicon, which is shown in Eq. (1.4), reacts further with the hydroxide ions formed by the reduction of water to form soluble silicon compounds as follows:

$$Si(OH)_2^{2+} + 4OH^- \rightarrow SiO_2(OH)_2^{2+} + 2H_2O \tag{1.6}$$

From the above equations, it is clear that the reaction depends on the amount of hydroxide ions, which is present in the solution. For KOH, Seidel demonstrated that 15 percent by weight KOH at 72 ^{o}C etches silicon at 55 μm/hr [10]. He also demonstrated that the etch rate depends on the fourth power of concentration of the water (hydroxide ions) in the solution. The etch rate of potassium hydroxide in the (110) plane is the maximum and the (111) plane is minimum. The etch rate of (100) plane in silicon crystal is 400 times slower than that of (111) plane of silicon. Masking materials used for KOH are Low Pressure Chemical Vapor Deposition (LPCVD) silicon nitride, thermally grown silicon oxide. Thermally grown silicon dioxide is also etched by KOH but its selectivity is low when compared to that of silicon. LPCVD silicon nitride shows almost zero etch rate in KOH. We can control the etching in KOH by doping or externally charging the sample. When silicon is doped, the relative distance between the charges on the surface is reduced, thus, reducing the etch rate in KOH. This also reduces the oxidation of the silicon on the surface of the substrate, thus reducing the etch rate. [10]

1.6 Summary

In this chapter, a brief discussion about some of the important terminology used in MEMS fabrication was discussed. The operating principle of the two different types of oxygenators namely the membrane and the bubble oxygenator was discussed. The application of MEMS fabrication principles to the fabrication of blood oxygenator were also discussed along with its advantages over the conventional blood oxygenators.

The following chapter discusses the design and modeling of the channel membrane oxygenator.

CHAPTER 2

DESIGN OF BLOOD OXYGENATOR

2.1 Design Criteria

Our aim is to, fabricate a micromachined nanoporous silicon membrane oxygenator, and mimic the working of natural lungs. For this, we need a device whose characteristics are comparable to natural lungs. Efficient oxygenation of blood requires:

Miniature size: The capillaries in the natural lung have a very narrow path for the flow of the blood. Because of the narrow path, the blood cells are in constant contact with the gas exchange membrane. This increases the gas exchange efficiency of the lungs. In order to keep the blood in constant contact with the membrane, we need to reduce the size of the blood flow path. This is achieved using micromachining techniques on silicon.

Mechanical strength: The membrane between gas and blood in natural lungs has enough mechanical strength, to withstand the pressure variations occurring in human body. The membranes in an artificial blood oxygenation system have to be mechanically stable to withstand the variation of blood pressure like the natural membrane, and should also withstand the pressure exerted on the membrane during the fabrication of the device. We can get a robust membrane with the established semiconductor technologies of thin film deposition and bulk micromachining.

Thin membrane for gas exchange: One of the biggest advantages of the natural lung is the thickness of the membrane for gas exchange, which is in the order of few microns. The thinnest polymer, which is available for usage, is in the order of

few tens of microns to few hundreds of microns in thickness. This reduces the rate of diffusion of gas through the pores on the membrane, which in turn reduces the gas exchange efficiency, and the oxygenation capability of the device. The thickness of the membrane in micromachined nanoporous silicon membrane oxygenator can be made to mimic that for the natural lungs using typical thin film deposition techniques.

Precise control of membrane porosity: One of the biggest shortcomings of currently used blood oxygenator is that the porosity of the polymer used as a membrane is not precisely controlled. The size and location of pores are not controlled. Moreover, the pores are not straight through the membrane. We can achieve the required porosity of the membrane with a high precision Focused Ion Beam (FIB) system in combination with control software Nabity Pattern Generation System (NPGS) or a Nanoimprinting system.

Biocompatibility: All implantable devices need to be biocompatible with the body, not to initiate the defense mechanisms. Many research groups have shown that silicon microdevices with micorpores are biocompatible in vitro and in vivo [11]. Though there seems to be a doubt over the biocompatibility of the materials, there appears to be means to make the blood channels biocompatible.

With the above design considerations for the lungs, the following design criteria were made for the micromachined nanoporous silicon membrane oxygenator:

- *The gas exchange efficiency of the fabricated membrane oxygenator should closely match to that for the natural lung.*
- *The ratio of the surface area of interaction to blood volume has to be balanced in the fabricated device.*
- *The surface area of blood/gas interaction has to be improved in order to increase blood oxygenation efficiency.*
- *The gas exchange membrane has to have precisely controlled porosity (i.e.)*

1. *The dimensions of the nanopores, which are to be drilled on the membrane, have to be precisely controlled,*
2. *The placement of the nanopores has to be accurate to get the required porosity.*

- *The membrane has to be robust, and should be able to withstand the pressure exerted by gas and blood during the exchange of gases from either side of the membrane.*

2.2 Materials

- *Silicon :* Silicon is to be used as the base material for the fabrication of the micromachined nanoporous silicon membrane oxygenator. It is used as the base material because of the ease of fabrication, and the desired qualities that meet the above requirements. For the fabrication of the channels and the test membrane, we used a (100) silicon wafer.
- *Silicon nitride :* Low Pressure Chemical Vapor Deposited (LPCVD) silicon nitride was the material used for fabricating the membrane. This was due to the following qualities of LPCVD silicon nitride:
  1. ease of deposition
  2. protects silicon during etching; therefore, there is no need for a separate masking material
  3. has very high yield strength and so it can withstand the required pressures. The yield strength of silicon nitride is reported to be around 1.39 GPa, the young's modulus has been reported to be 304 GPa.
- *Photoresist*: The photoresist used for masking during patterning of silicon nitride is SU8-2010. SU 8-2010 was used because of the following reasons:
  1. selectivity of nitride to SU8 when etched in DRIE etcher is high

2. higher aspect ratio is achievable using SU8
3. vertical side walls formed gives us a sharper edge of the feature.

- *Potassium Hydroxide*: Potassium hydroxide is used to etch the silicon in the substrate to form the membrane. We use potassium hydroxide because of the following reasons:
  1. anisotropically etch silicon to make the channels
  2. higher etch rates for silicon when compared to others etching solutions
  3. etched surfaces are smooth
- *Gold*: Gold was sputtered on the membrane to reduce the charging effect on the membrane while drilling pores using FIB. The thin layer of gold (100 - 150 Angstroms) acts as the conducting medium on the top layer of the membrane thus, removing charge from the membrane. This helps in better focusing on the membrane.

Calculation of the design parameters were based on the following assumptions

- Thickness of wafer was assumed to be 40 μm,
- The thickness of the membrane was assumed to vary from 0.8 - 1 μm
- The variations in uniformity of the silicon nitride is less that 5%.

Other materials, which were experimented, have been listed in the Table 2.1. The wet etching solution refers to the etching solution used for etching the substrate silicon to form the membrane, and the etching process given below:

- The concentration of KOH solution was 30% by weight. This solution was prepared by adding KOH flakes to DI water. The KOH flakes were 180 grams and the DI water was 420 ml to obtain a 600ml of 30% KOH solution. This percentage was chosen in order to obtain a relatively smooth surface finish after etching and to achieve maximum etch rate. The etch rate was found to vary

from 1.4 μm to 0.7 μm over time, due to the loss of hydroxide ions in the solution (please refer to Chapter 1).

- The temperature of the etch solution was maintained at 85^oC. The temperature was maintained close to the boiling point of water, as we did not want the water to evaporate from the solution, thus further depleting the hydroxide ions.

Table 2.1. Materials experimented for fabrication

Membrane material	**Masking material**	**Etching method**	**Reason for failure**
Sputtered Si_3N_4	Self	Wet etching solution	1. Pin holes in sputtered Si_3N_4 2. Silicon richness of sputtered Si_3N_4
Sputtered Si_3N_4	Sputtered Ti	Wet etching solution	1. Pin holes in sputtered Ti 2. Silicon richness of sputtered Si_3N_4
Sputtered Si_3N_4	Evaporated Ti	Wet etching solution	1. Pin holes in evaporated Ti 2. Silicon richness of sputtered Si_3N_4
Sputtered Si_3N_4	Evaporated Cr/Au	Wet etching solution	The lateral etching of silicon could have etched Cr thus lifting off Au thus exposing sputtered Si_3N_4
PECVD Si_3N_4	Self	Wet etching solution	Silicon richness of PECVD Si_3N_4
PECVD Si_3N_4	Sputtered Ti	Wet etching solution	1. Pin holes in Sputtered Ti 2. Silicon richness of PECVD Si_3N_4
PECVD Si_3N_4	Evaporated TI	Wet etching Solution	1. Pin holes in evaporated Ti 2. Silicon richness of PECVD Si_3N_4
PECVD Si_3N_4	Evaporated Cr/Au	Wet etching Solution	The lateral etching of silicon could have etched Cr and thus lifting off Au thus exposing PECVD Si_3N_4

2.3 Membrane Design

2.3.1 Silicon membrane

Silicon membranes are realized by simultaneous etching of the front and the backside of the silicon wafer. Silicon when etched using potassium hydroxide, etches anisotropically. When we carefully place rectangular openings on the front and backside of the wafer, we will be able to fabricate a membrane of required thickness. The membranes will be at an angle of 54.7 to the wafer plane, since KOH is an anisotropic etching agent, preferential to (100)direction over (111) direction.

The fabrication of silicon membrane begins with the deposition of LPCVD silicon nitride on a clean (100) silicon wafer. A suitable photoresist is spin casted on the front side of the wafer. The photoresist is then patterned on front side to form rectangular/square features by exposing it to UV light. After patterning the photoresist, nitride on the front side of the wafer is removed by dry etching process. Using a very similar process and with precise alignment, silicon nitride on the backside of the silicon wafer is etched. Subsequent to the removal of the nitride, the wafer is placed in a solution of potassium hydroxide, which etches silicon anisotropically [12]. This is the general procedure to fabricate silicon membranes. In our case, we dope silicon with high concentration of p-type impurities before depositing silicon nitride. This will act as an etch stop for silicon etching using potassium hydroxide. The doped silicon will give the channel added mechanical stability.

Figure 2.1(a) shows the cross-section of the wafer after dry etching the nitride. There are two parameters, namely d and W which we need to consider when fabricating the membrane is shown in Figure 2.1(a). The width of the channel and the depth of the channel are determined by the dimensions of d and W. Figure 2.1(b) shows the cross-section of the wafer etching the wafer in KOH. The thickness and width of

the membrane are given by, T_w and W_m respectively. The thickness of the membrane and the width of the membrane depend on the values of d, W, the angle $54.7(\theta)$, the thickness of the wafer(T_w), the rate and time of etching. The rate of silicon etching in KOH was found to be 1.4 μm/min from experimental data. The thickness of the membrane and the width of the membrane are given by [12]

$$T_m = \left[d + \frac{T_w}{tan\theta} - W - 2rt \right] cos(\theta) \tag{2.1}$$

$$W_m = \frac{W}{2cos(\theta)} + \frac{rt}{sin\theta cos\theta} \tag{2.2}$$

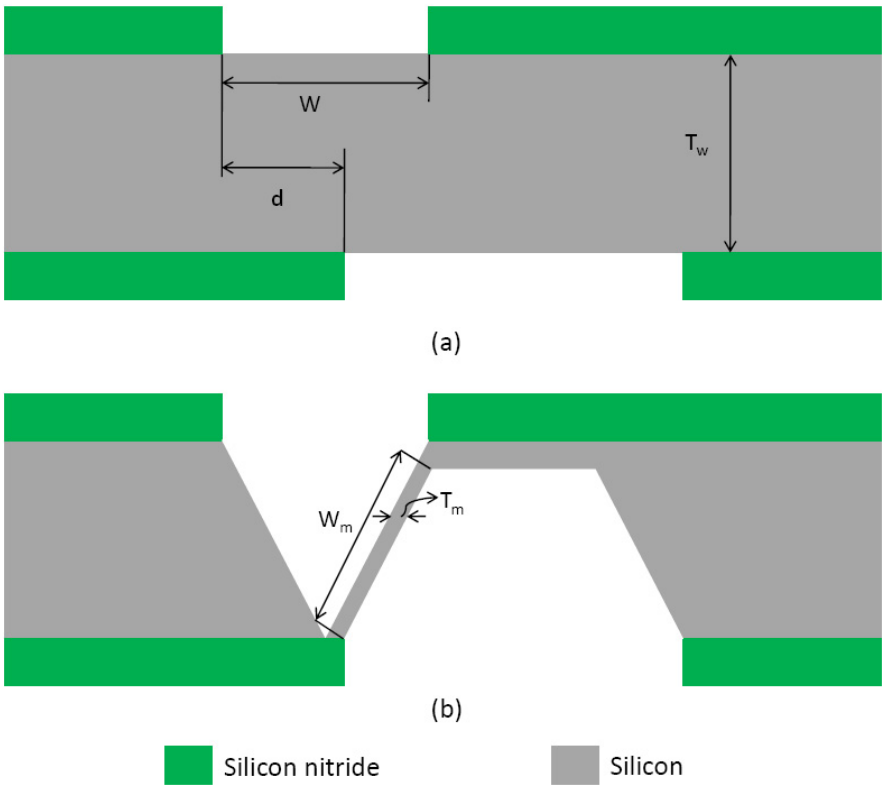

Figure 2.1. (a) Cross-section of substrate after patterning of silicon-nitride;(b) Cross-section of substrate after etching in KOH.

2.3.2 Silicon nitride membrane

The design of silicon nitride membrane is relatively simpler when compared to design of silicon membrane. To fabricate a membrane using silicon nitride, we use the same principle of bulk micromachining as we used in the case of silicon membranes. The process for fabricating silicon nitride membranes is as follows: silicon nitride is deposited on both sides of the wafer using LPCVD technique. The deposited nitride is patterned, and dry-etched. The patterned silicon nitride is used as a mask while bulk micromaching of silicon using KOH. The etching of silicon is done until the silicon in the exposed regions is completely etched. Since, silicon nitride is not etched by KOH; we are left with a membrane of silicon nitride, after etching of silicon is complete. Thus, the etching of silicon using KOH leaves a membrane of silicon nitride, suspended in the middle and supported on the four sides by the wafer. The fabrication of silicon nitride membranes is discussed in detail in Chapter 3 with respect to our specific design.

2.4 Silicon channel designs

2.4.1 Dome Channel

The dome channel is a single gas channel and a single blood channel design. The gas channel is realized on silicon by bulk micromachining of silicon, and the blood channel, by surface micromachining. The dome channel design is a single wafer process and is comparatively easy to fabricate. The height of the blood and gas channels can be adjusted to optimize the blood to gas volume ratio. The surface area of interaction between the blood and the gas depends on the height of the gas channel. Figure 2.2 depicts the stacked model of the dome channel design.

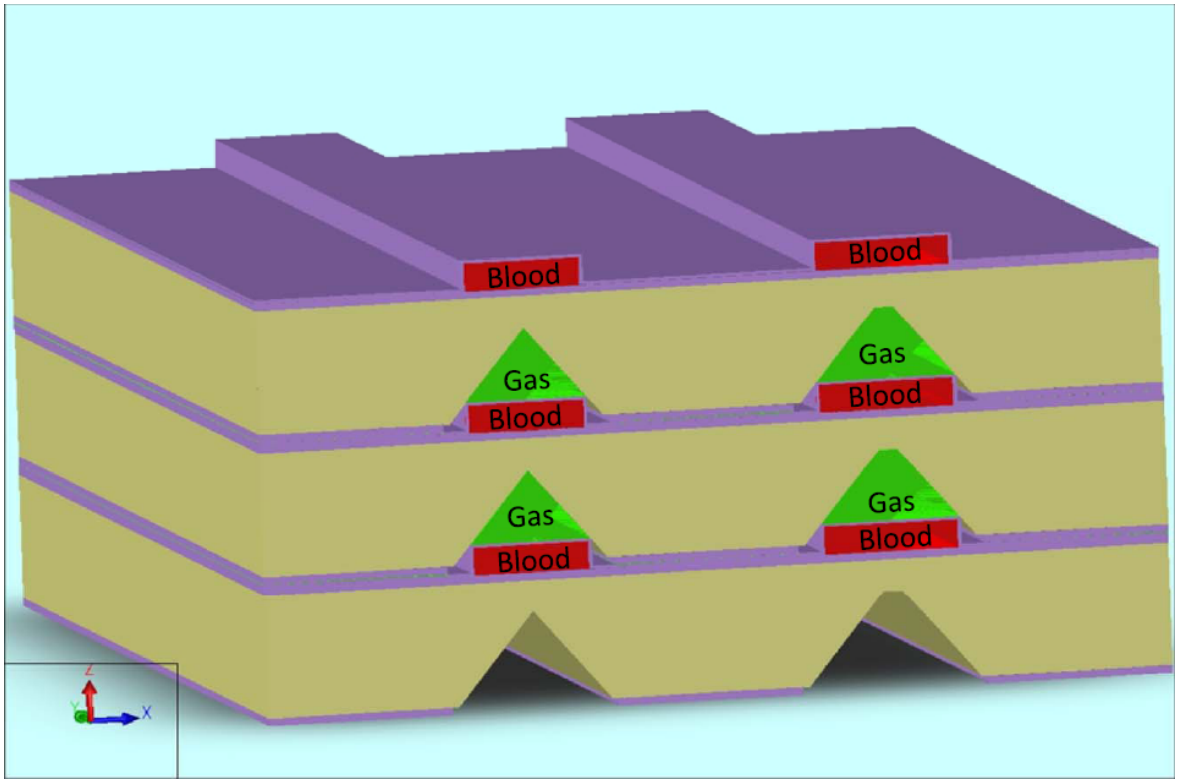

Figure 2.2. Stacked model of Dome channel design.

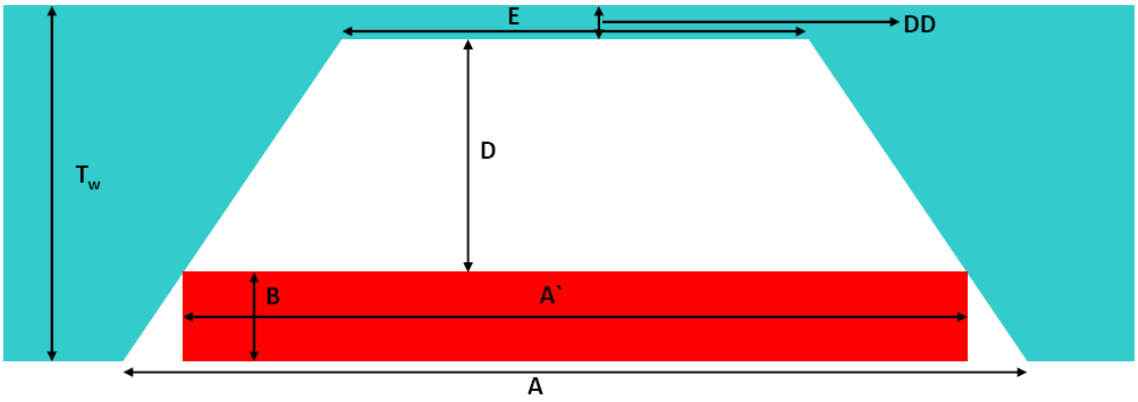

Figure 2.3. Cross section of Dome channel design.

Figure 2.3 shows the cross-section of the dome channel design. The different parameters indicated in Figure 2.3 are listed in the Table 2.2, with the parameters identified as independent, fixed, and dependent. The independent parameters are those whose values were varied to model the design, and to obtain a balance between the blood and gas volume. The fixed parameters were kept as constant during the calculation. The values of the dependent parameters were calculated, to optimize the design.

Table 2.2. Parameters for Dome channel design

Parameter	**Description**	**Variation**	**Value/Range**
T_W	Thickness of wafer	Fixed	$40\mu m$
A	Width at bottom	Dependent	
$\bar{A}$	Width of blood channel	Dependent	
D	Height of gas channel	Dependent	
B	Height of blood channel	Independent	$5\mu m, 8\mu m, 10\mu m$
DD	Diffusion depth	Independent	$8\mu m$
E	Width of gas channel	Independent	$0 - 25\mu m$ in steps of 0.1μm

The dome channel design was modeled to obtain balanced blood to gas volume ratio. The independent parameters were varied for a suitable range of values, and the dependent parameters were calculated. The width of gas channel at top (E) was varied from 0 μm to 25 μm in steps of 0.1 μm, and the corresponding values for the dependent parameters were calculated. The values assumed for fixed parameters are listed in Table 2.2. As far as ease of fabrication, and mechanical strength are concerned, the diffusion depth (DD) was assumed to be 8 μm. The height of blood channel (B) was assumed to be 5 μm, 8 μm, and 10 μm for different sets of calculations. The Dome channel cross-section is shown in Figure 2.3. The height of the

gas channel (D) is the first dependent factor, which we need to consider. The value of the height of the gas channel depends on two independent parameters, namely the height of the blood channel (B), and the diffusion depth (DD).

$$D = T_w - B - DD \tag{2.3}$$

The volume of the blood channel, and the gas channel are calculated per unit length, perpendicular to the cross section shown in Figure 2.3. The volume of the blood channel per unit length is the area of the rectangle, which forms the channel. In our case, the length of the rectangle is the width of the blood channel, which is $\bar{A}$, and the breadth is height of the blood channel B. The volume of the blood channel *V1* is given in Equation 2.5. The height of the blood channel (B) is an independent parameter. The values of B, which were used for calculations, are shown in Table 2.2. The width of the blood channel $\bar{A}$ is a dependent parameter. The value of $\bar{A}$ depends on the width of the gas channel, and the height of the gas channel as the angle is fixed for the gas channel. The value of $\bar{A}$ is calculated using Equation 2.4.

$$\bar{A} = E + \left\{ 2 * \left[\frac{D}{Tan(54.7)} \right] \right\} \tag{2.4}$$

$$V1 = \bar{A} * B \tag{2.5}$$

The volume of the gas channel per unit length ($V2$) is the area of the trapezium, which is formed with the width of the blood channel ($\bar{A}$) as base and the width at top of gas channel (E) as the top. The area of the gas is given as

$$V2 = D * \frac{\left(\bar{A} + E\right)}{2} \tag{2.6}$$

One of the important design criteria is to obtain a balanced blood/gas volume ratio. To obtain this in dome channel design, we vary the values for the height of the blood channel (B), and the width of the gas channel (E). Change in values of either B

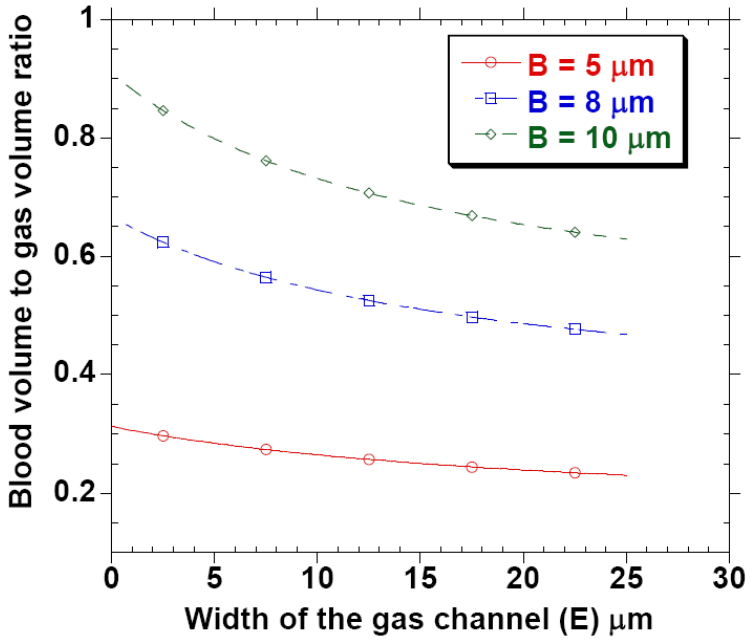

Figure 2.4. Variation of the blood/gas volume with respect to change in width of gas channel (E).

or E modifies the value of blood to gas volume ratio. The blood volume is directly proportional to B. The gas volume is directly proportional to the value of E and inversely proportional to the value of B. As we change the value of B it alters the height of the gas channel (D) (please refer Equation 2.3). The change in the height of the gas channel affects the volume of the gas channel. If B is increased, then the height of the gas channel is decreased as the other parameters, the diffusion depth, and thickness of wafer are held constant. If the value of B is decreased, the height of the gas channel increases, thus increasing the gas channel volume per unit length. The variation of the blood to gas volume ratio with respect to E, A, and $\bar{A}$ is shown in the Figures 2.4, 2.5, and 2.6 respectively.

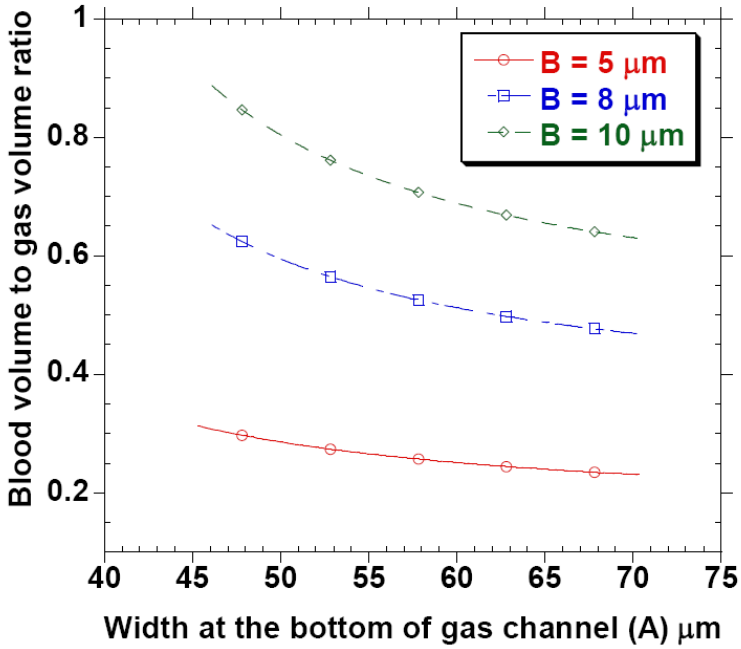

Figure 2.5. Variation of blood/gas volume ratio with respect to width of the gas channel (A).

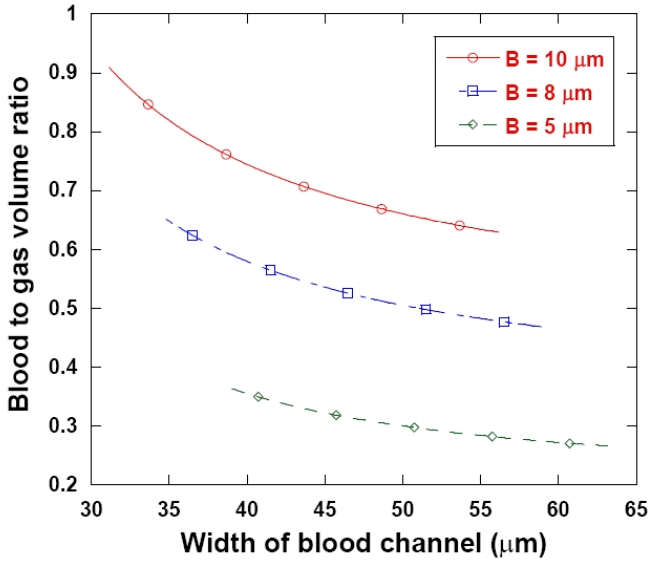

Figure 2.6. Variation of blood/gas volume with respect to width of the blood channel ($\bar{A}$).

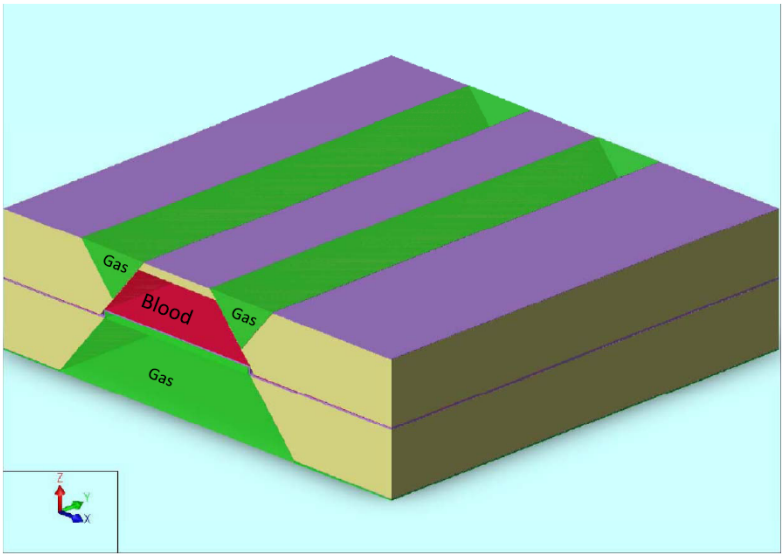

Figure 2.7. Stacked model of rooftop/dome channel.

2.4.2 Rooftop/Dome Channel

The Rooftop/dome channel design is a single blood channel, and three-gas channel design. The rooftop/dome channel is a two-wafer design. The blood channel and two of the gas channels are realized in silicon using bulk micromachining of silicon. The third gas channel is accomplished using, a combination of bulk and surface micromachining techniques. The depth of two gas channels, can be varied by changing the value of W. The height of the third gas channel depends on the thickness of the wafer (T_w), and thickness of the sacrificial layer deposited (T_g). Figure 2.7 shows the stacked model of the rooftop/dome channel design.

Figure 2.8 illustrates the cross-section of the rooftop/ dome channel design. The different parameters indicated in the Figure 2.8 are listed in the Table 2.3. The independent parameter width of gas channel at top *(W)* was varied from 10 μm to 75 μm in steps of 0.5 μm. The corresponding values of the dependent parameters were calculated. The other independent parameters like the diffusion depth *(DD)*, width of blood channel at top *(E)* in wafer 1, and the height of the gas channel (T_g) in

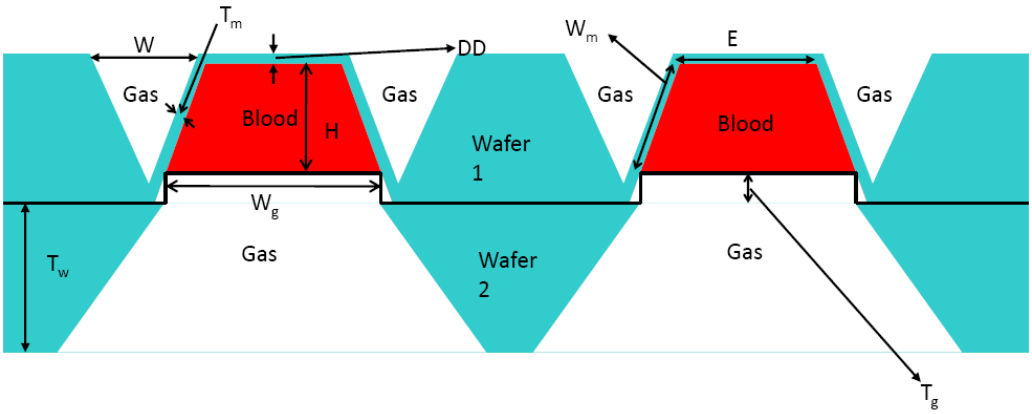

Figure 2.8. Cross-section of rooftop/dome channel.

Table 2.3. Parameters for Rooftop/ dome channel design

Parameter	**Description**	**Variation**	**Value/Range**
T_w	Thickness of wafer	Fixed	$40\mu m$
T_m	Thickness of membrane	Fixed	$0.8\mu m$
W	Width of gas channel at the top	Independent	10 - $75\mu m$ in steps of $0.5\mu m$
T_g	Height of gas channel (wafer2)	Independent	$5\mu m$
DD	Diffusion depth	Independent	$8\mu m$
E	Width at top of blood channel	Independent	$50\mu m$
H	Height of blood channel	Dependent	
W_g	Width of blood channel	Dependent	
W_m	Width of membrane	Dependent	

wafer 2 were taken as best-guess values. Table 2.3 gives the values assumed for fixed parameters. The depth of the gas channels on wafer 1 is an important parameter, which we need to consider carefully. This is because, the volume of the gas channel, and the surface area of interaction of the blood to gas also depend on the gas channel depth. The gas channel depth is directly proportional to the gas channel width at the top *(W)*. When silicon is etched in KOH, it is etched anisotropically forming a V-groove in silicon. The anisotropic etch forms an angle of 54.7^o to the plane of the

wafer. Thus, the depth of the gas channel depends on the width of the gas channel W, and the tangent of the angle 54.7^o. The depth of the gas channel $D1$ can be calculated using Equation 2.7.

$$D1 = 0.5 * \left(\frac{W}{Tan54.7}\right) \tag{2.7}$$

The volume of the blood channel per unit length ($V3$) is the area of the trapezium formed by the bulk micromaching of silicon in wafer1. The base of the blood channel is formed by the width of the gas channel in wafer 2. The width of the gas channel in wafer 2, depends on the height of the gas channel T_g, and the width of the blood channel at top *(E)* in wafer1.

$$V3 = 0.5 * H * (E + W_g) \tag{2.8}$$

The surface area of interaction of the blood volume to gas volume also depends on the depth of the gas channels in wafer 1. As the value of depth of the gas channel increases, the volume of the gas channel increases, this increases the surface area of interaction with blood channel. Figure 2.9 shows the variation of the blood/gas volume ratio, as the width of gas channel *(W)* is changed. Figure 2.9 clearly shows that, as the value of W is increased, the ratio of blood/gas volume decreases. This is because when W increases, the depth of the gas channel increases, which increases the volume of gas channel per unit length. The value of W does not affect the value of the blood volume per unit length, thus decreasing the value of blood/gas volume ratio overall.

Figure 2.10 shows the variation of the ratio of surface area of interaction to the blood volume, as a function of the width of the gas channel *(W)*. Surface area of interaction here is the area common to blood and gas volume. As the value of W increases, the depth of the gas channel increases which increases the width of the

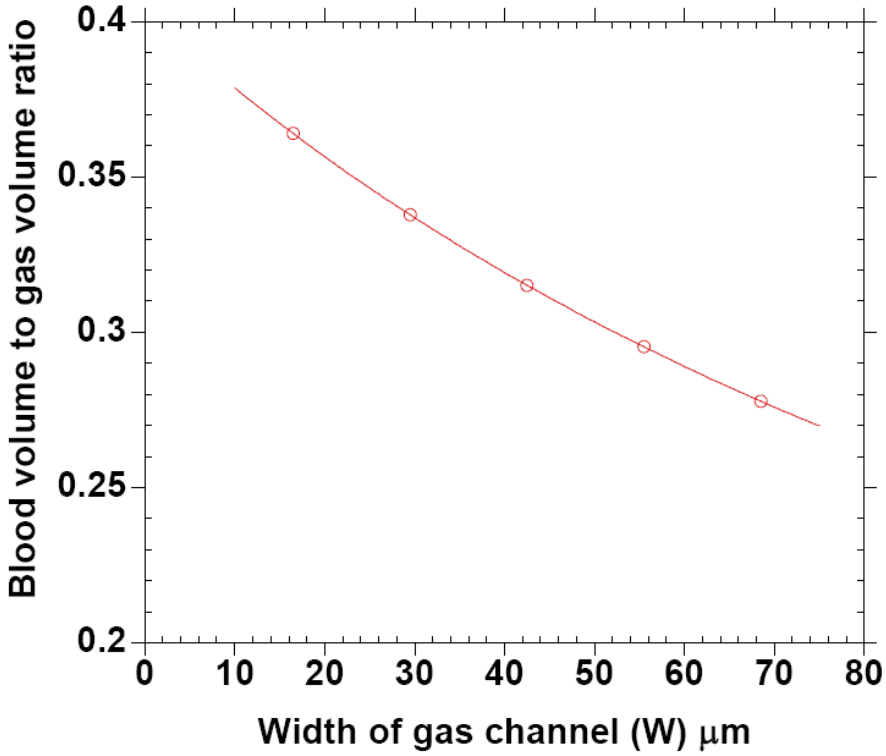

Figure 2.9. Variation of blood/ gas volume to width of gas channel at top *(W)*.

membrane. This, in-turn, increases the area of interaction of the blood volume with the gas volume. Thus, as the value of W increases the ratio of surface area to blood volume increases.

2.4.3 Rooftop channel I

The Rooftop channel I has a single blood channel for two gas channels. This design is very similar to the Rooftop/ dome channel. Unlike, the Rooftop/dome channel, which is a two-wafer design, the Rooftop channel I is a single wafer design. The blood channel and the gas channel both are realized using bulk micromachining of silicon. Figure 2.11 exhibits the stacked model of the Rooftop channel I. The red channel indicates the blood channel and the green channels indicates the gas channels.

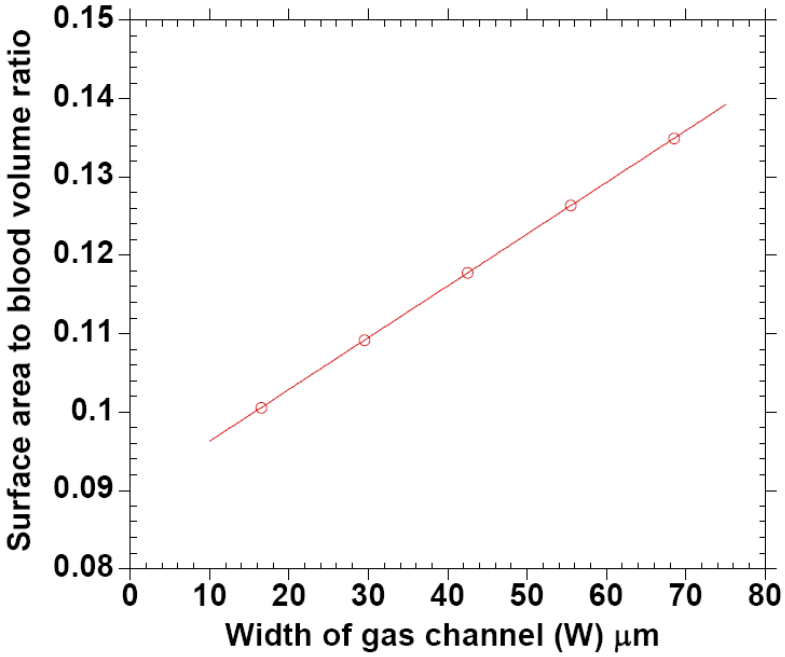

Figure 2.10. Variation of surface area of interaction with respect to the variation in width of the gas channel at top *(W)*.

Figure 2.12 shows the cross-section of the rooftop channel I. The different parameters are indicated in the Figure 2.12 are listed in the Table 2.4.

The independent parameter, the gas channel width at top *(W)* was varied from 10 μm to 56.5 μm in steps of 0.5 μm. The other independent parameters like the diffusion depth *(DD)*, width of blood channel at top *(E)* and the thickness of the membrane (T_m) were assumed to be of a suitable value. The diffusion depth was assumed to be 7 μm; the width at top of the blood channel was assumed to be 50 μm and thickness of the membrane was assumed to be 0.8 μm. The parameter which requires careful consideration in this design is the depth of the gas channel which is a function of the independent parameter *W*. This is because, silicon is etched anisotorpically using KOH to form the gas channels. As discussed earlier in Chapter 1, the depth of etching, when silicon is etched anisotropically depends on the width

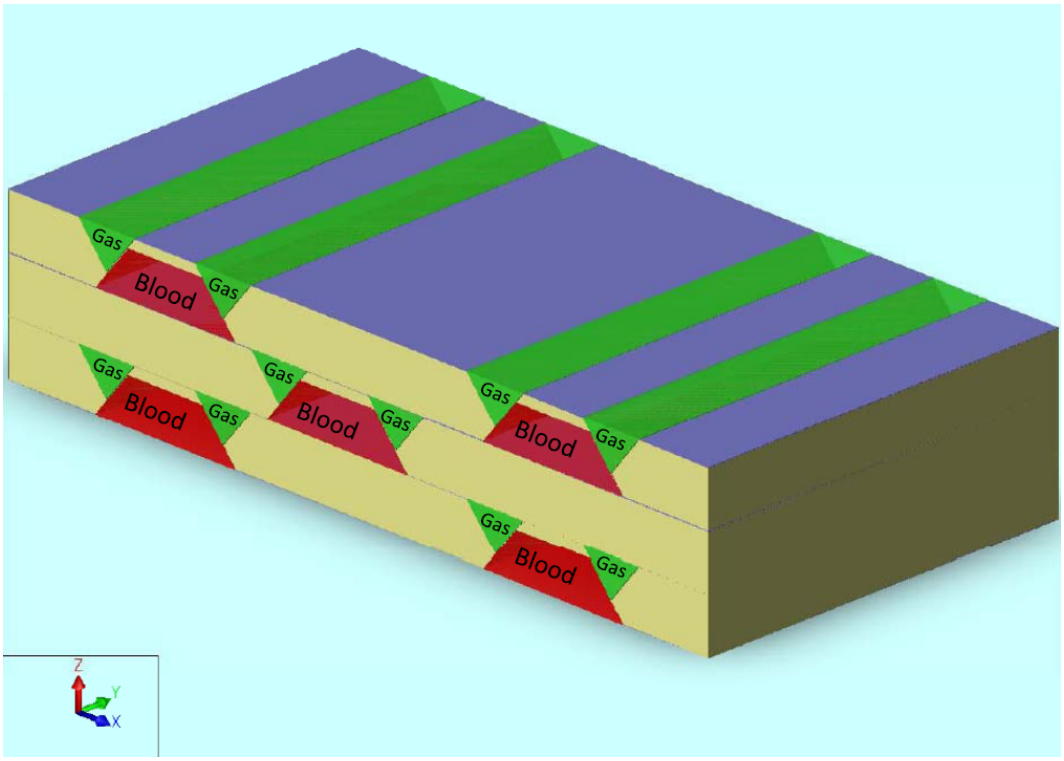

Figure 2.11. Stacked model of Rooftop channel I.

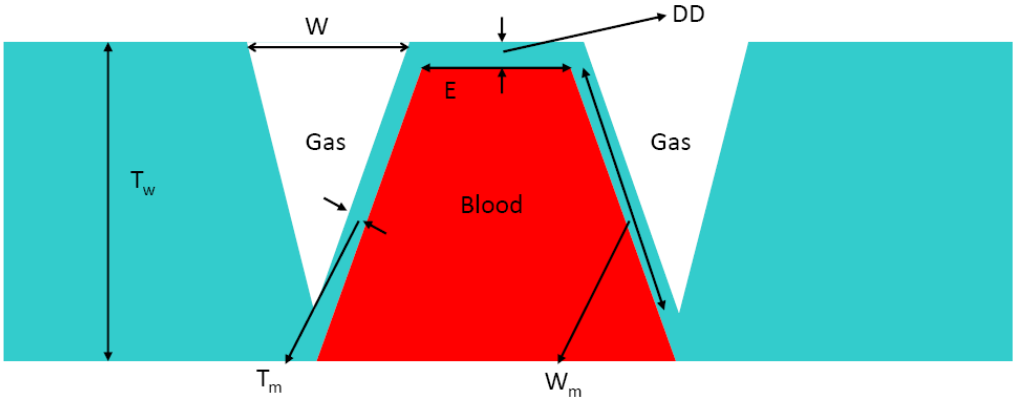

Figure 2.12. Cross-section of Rooftop channel I.

Table 2.4. Parameters for Rooftop channel I design

Parameter	**Description**	**Variation**	**Value/Range**
T_w	Thickness of wafer	Fixed	$40\mu m$
T_m	Thickness of membrane	Fixed	$0.8\mu m$
W	Width of gas channel at the top	Independent	10 - $56.5\mu m$ in steps of $0.5\mu m$
T_g	Height of gas channel (wafer2)	Independent	$5\mu m$
DD	Diffusion depth	Independent	$8\mu m$
E	Width at top of blood channel	Independent	$50\mu m$
W_m	Width of membrane	Dependent	

of opening at top (pleas refer to Chapter 1, section 1.4.2). Thus, the depth of gas channel depends on the gas channel width *W*. The volume of blood channel per unit length is the area of the trapezium. The area of the trapezium is dependent on the blood channel width at the top *(E)*, and the blood channel height. The blood channel height depends on the diffusion depth *(DD)*, and the wafer thickness (T_w). The variation of the blood to gas volume ratio with respect to the variation of the width of the gas channel *(W)* is shown in Figure 2.13. It can be seen from Figure 2.13, that the ratio of blood to gas volume is much higher when compared to the other designs, and our design requirement. The blood to gas volume ratio varied from 3400% to 150% when W is changed from 10 μm to 56.5 μm. The variation of ratio of surface area of interaction to the blood volume with respect to the variation in the width of the gas channel is shown in Figure 2.14. From Figure 2.14 it is clear that, the variation of ratio of surface area of interaction to blood volume is directly proportional to the value of *W*. As the value of W increases the depth of the gas channel increases. As the channel becomes deeper, the membrane area of interaction increases. Thus, the ratio surface area of interaction to the blood volume increases with increase in *W*.

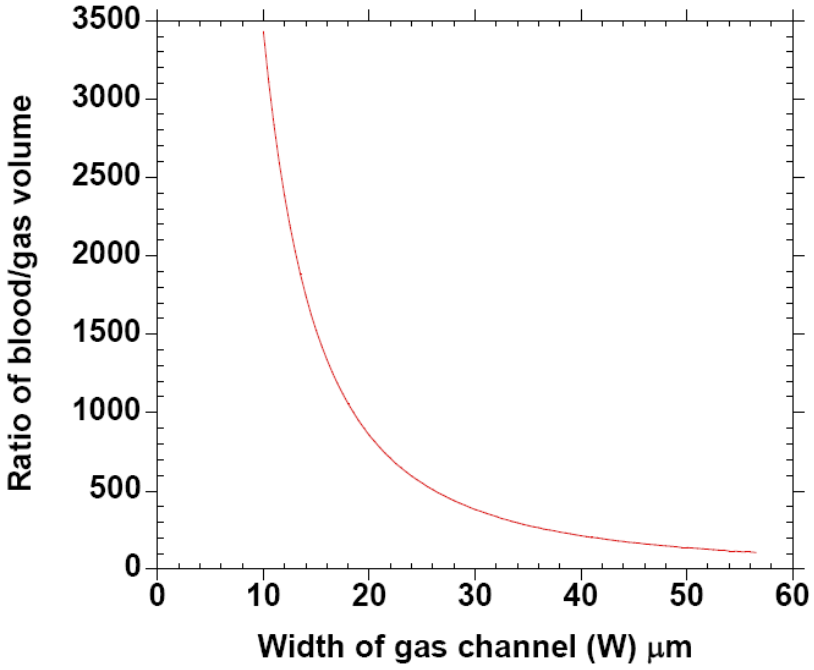

Figure 2.13. Variation of blood to gas volume ratio with change in the gas channel width *(W)*.

2.4.4 Rooftop Channel II

The Rooftop channel II has a single blood channel for three-gas channels. This design is a combination of Rooftop channel I, and the Dome channel design. The fabrication of the Rooftop channel II is a single wafer process. The blood channel and two of the gas channels are realized by bulk micromachining of silicon using KOH. The third gas channel is realized by a combination of thin film deposition and surface micromachining techniques. The blood channel height and the gas channel height can be varied. Figure 2.15 depicts the stacked model of the Rooftop channel I. Figure 2.16 shows the cross-section of the Rooftop channel II. The different parameters indicated in Figure 2.16 are listed in the Table 2.5 and their variations are listed as independent, fixed, and dependent.

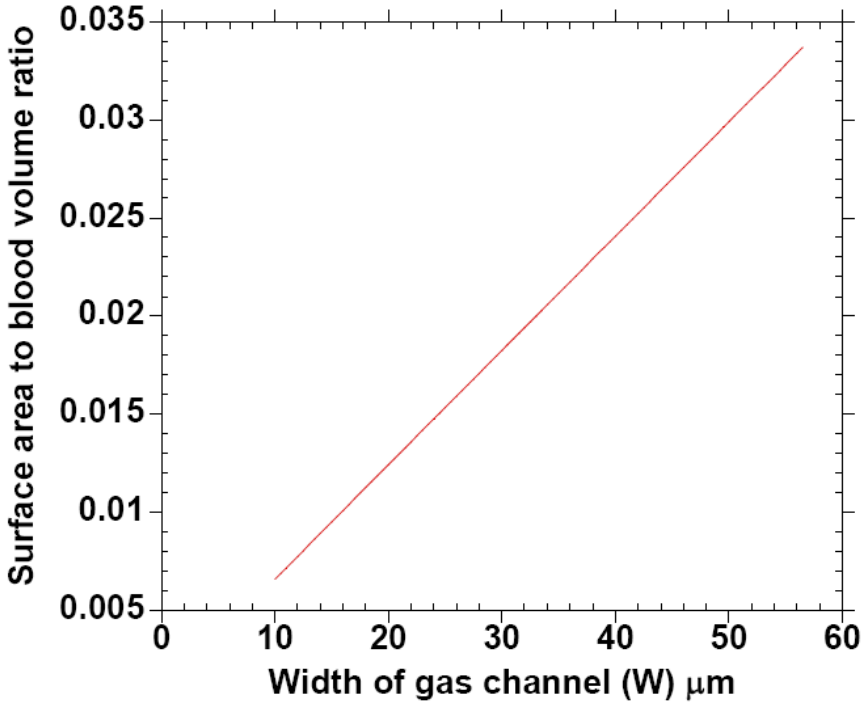

Figure 2.14. Variation of ratio of surface area to the blood volume with respect to the change in the width of the gas channel.

Table 2.5. Parameters for Rooftop channel II design

Parameter	**Description**	**Variation**	**Value/Range**
T_w	Thickness of wafer	Fixed	$40\mu m$
T_m	Thickness of membrane	Fixed	$0.8\mu m$
W	Width of gas channel at the top	Independent	10 - $75\mu m$ in steps of $0.5\mu m$
T_g	Height of gas channel	Independent	$8\mu m$
DD	Diffusion depth	Independent	$8\mu m$
E	Width at top of blood channel	Independent	$50\mu m$
W_m	Width of membrane	Dependent	

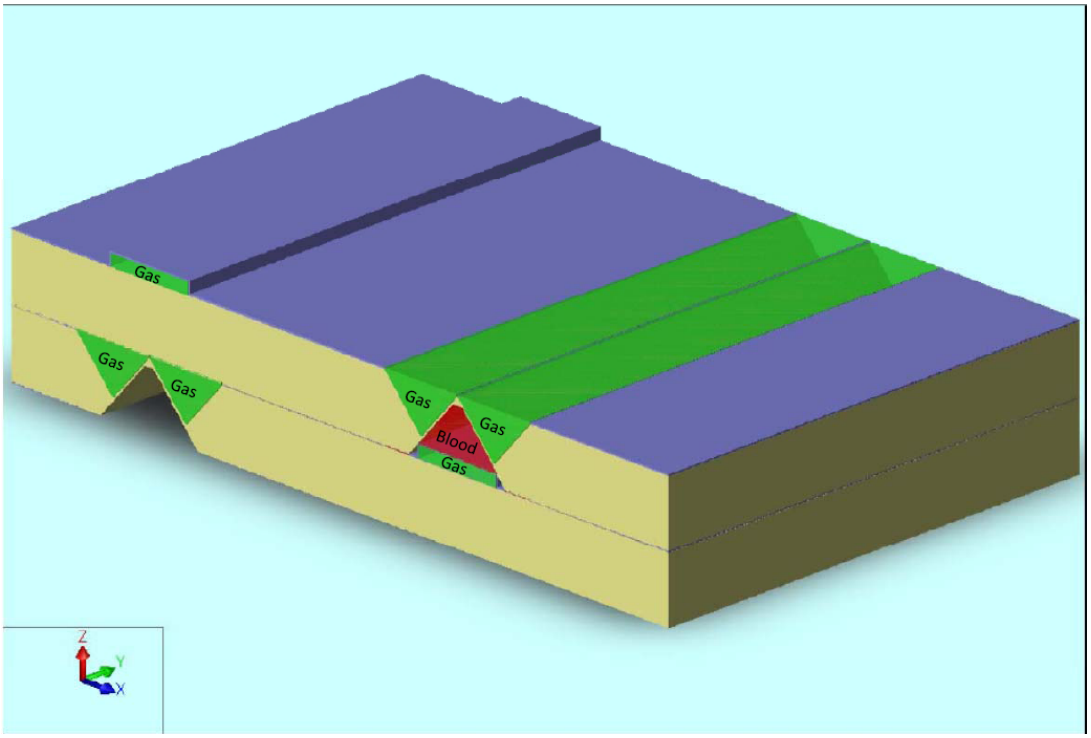

Figure 2.15. Stacked model of rooftop channel II.

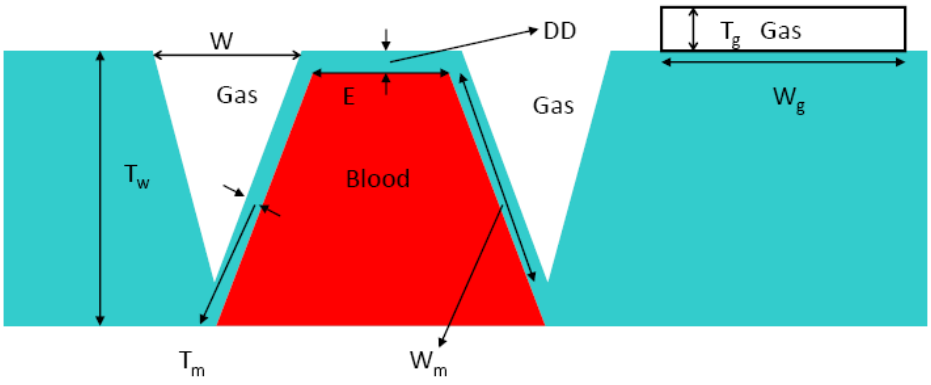

Figure 2.16. Cross section of Rooftop channel II design.

The independent parameter width of gas channel at top (W) was varied from 10 μm to 75 μm in steps of 0.5 μm. The diffusion depth was assumed to be 5 μm, width at top of the blood channel was assumed to be 50 μm, and thickness of the membrane was assumed to be 0.8 μm . As discussed in earlier section (please refer to Chapter 1, Section 1.4.2) the depth of the gas channels fabricated using bulk micromachining, depends on the value of W and the tangent of angle 54.7. The total volume of the gas channel is the sum of the volume of the two gas channels and the volume of the gas channel from the gas channel inside the blood channel, which is the rectangular gas channel. The volume of blood channel per unit length is the area of the trapezium, which is dependent on the width of the blood channel at the top *(E)*, an independent parameter, and the height of the blood channel. The variation of the blood to gas volume ratio, with respect to the variation of the width of the gas channel is shown in Figure 2.17. It can be seen from Figure 2.17 that the ratio of blood to gas volume is much optimized when compared to other designs and meets our design requirements. The blood to gas volume ratio varied from 156% to 15% for variation in W from 10 μm to 75 μm. The ratio of surface area of interaction to the blood volume increases as we increase the value of W.

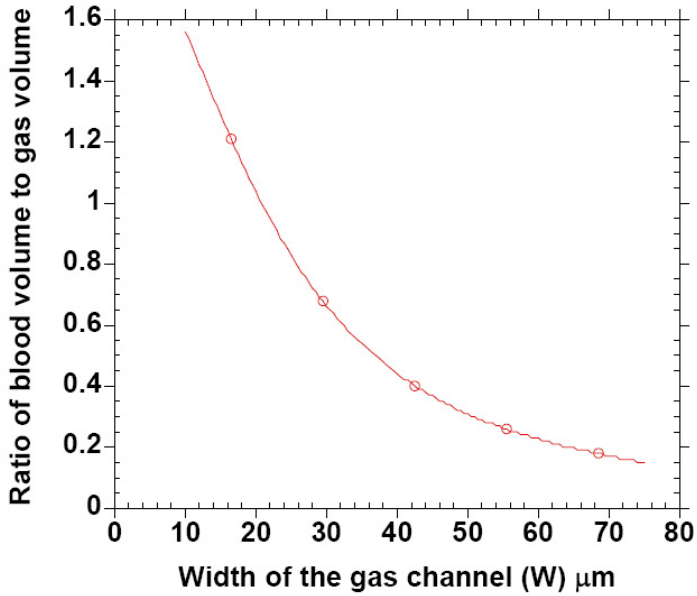

Figure 2.17. Variation of ratio of blood/gas volume with respect to the change in width of gas channel (W).

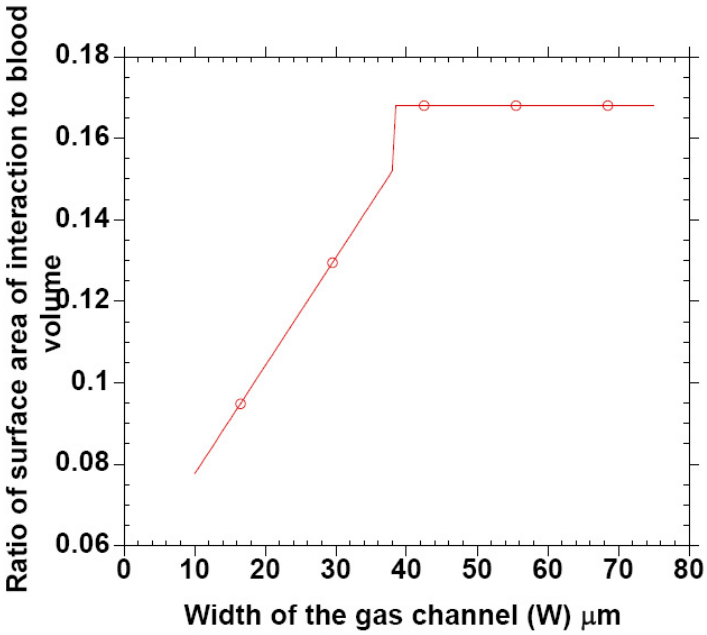

Figure 2.18. Variation of ratio of surface area of interaction to blood volume with respect to the change in width of gas channel (W).

2.5 Comparison of different Channel designs

The different channel design, which were discussed in earlier sections, have been listed below in the Table 2.6 for comparison. Table 2.6 gives us a comparison of the channel designs for the blood/gas volume ratio, and the ratio of surface area of interaction to blood volume. Table 2.6 also shows the number of wafers required to fabricate the device. When we consider the Dome channel, the ratio of blood/gas volume in the dome channel varies from 90% to 62% with variation in design parameters. The range of values obtained for the blood/gas volume ratio is optimal for the design and satisfies our design requirements. The ratio of surface area of interaction to the blood volume is 0.1 μm. This value is a constant immaterial of the change in the free parameters. In Rooftop/Dome channel design the ratio of blood/gas volume ranges from 34%-25%. This does not meet our requirements, as the ratio is too low. The ratio of surface area of interaction to blood volume varies from 0.096-0.139 μm. The ratio of the surface area of interaction to blood volume is high when compared to the Dome channel. However, the drawback of this design is that the ratio of blood/gas volume is very small while the ratio of surface area of interaction to the blood volume is high. This combination makes the design less efficient. The other drawback is that the design is a 2-wafer process and needs precise alignment, which complicates the fabrication. The Rooftop channel design has two sub-designs namely the Rooftop channel design I, and Rooftop channel design II. In the Rooftop channel design I the ratio of blood/gas volume varies from 3400% - 150%. The ratio of blood/gas volume is too high. This will lead to improper oxygenation of blood. The other important quantity, the ratio of surface area of interaction to the blood volume varies from 0.0065 - 0.033 μm. This is too small for the design criteria. The second design is the Rooftop channel design II. This design has the ratio of blood/gas volume ranging from 156% to 15%, thus giving us a wide range of the ratio blood/gas volumes to

operate with. The ratio of surface area of interaction to blood volume is also high for this design, ranges from 0.077-0.168 μm. Rooftop channel design II is a single wafer process, and needs precise alignment to realize in silicon. Thus, from Table 2.6 it is clear that the designs, which meet our requirements, are the Dome channel, and the Rooftop channel II.

Table 2.6. Comparison of channel design parameters

Design	**Ratio of blood/ gas volume(%)**	**Ratio of surface area of interaction to blood volume** (μm^{-1})	**No.of Wafers**
Dome channel	90 - 62	0.10	1
Rooftop/Dome channel	34 - 25	0.096 - 0.139	2
Rooftop channel I	3400 - 120	0.0065 - 0.033	1
Rooftop channel II	156 - 15	0.077 - 0.168	1

2.6 Summary

This Chapter discussed the design, and modeling of different channel designs for the membrane oxygenator. Different membrane oxygenators were modeled, and the best were opted for further analysis, and fabrication. The important requirements, which were considered for the selection of the designs were: 1. ratio of blood to gas volume, and 2. ratio of surface area of interaction to the blood volume. The selected designs had range of values, which covers the optimized value for both design requirements. In the next Chapter, the fabrication of prototype, and mechanical testing are discussed.

CHAPTER 3

FOCUSED ION BEAM SYSTEM

3.1 Introduction

Generally, a Focused Ion Beam system (FIB) is used for preparing samples for Transmission Electron Microscopy (TEM), or for characterizing the samples. The FIB system at UTA NanoFAB center is coupled with a Nanometer-Pattern Generation System (NPGS). The NPGS is commercially available software, which can be used to control the beam movement of the FIB system. Using NPGS, we are able to command the FIB system to make the patterns, which we input. The basic block diagram of the operation of the FIB system connected to the NPGS system is shown in Figure 3.1.

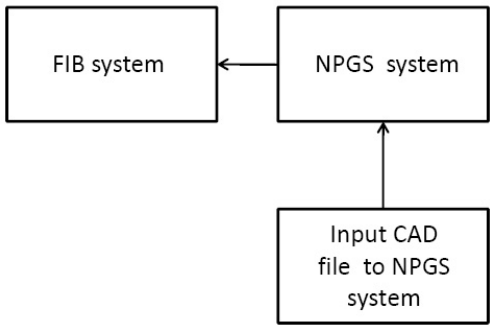

Figure 3.1. Block diagram of operation of NPGS and FIB system.

Figure 3.2 gives the basic configuration of the FIB system. The FIB system consists of two major parts namely the source (source of ions), and the beam column which houses parts for focusing, alignment, and an arrangement to move the beam.

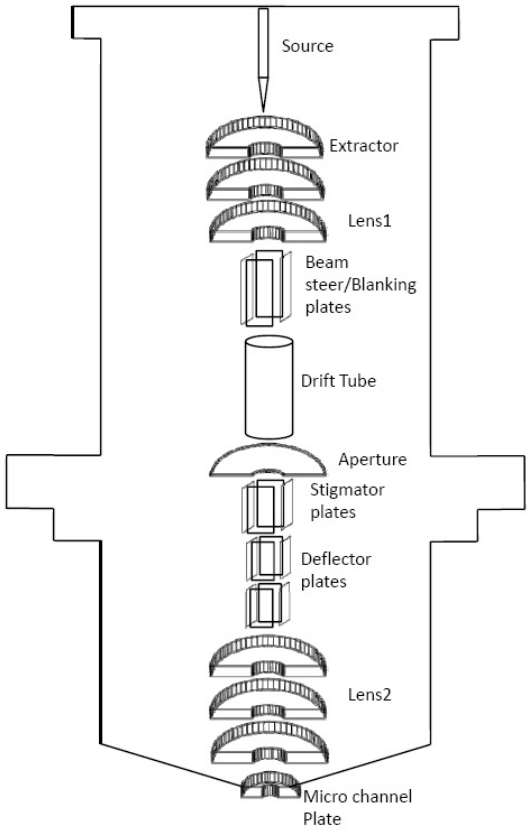

Figure 3.2. FIB system.

3.2 Source

The source for the FIB is a Liquid Metal Field Ionization Source (LMIS). The source consists of an emitter and a heater. The emitter is of the shape of a needle, and the end radius of the needle is around 10 μm. The needle is coated with a metal film, which has high surface tension and low melting point. In order, to extract ions from the source, the needle is heated, and subjected to a high voltage. The high positive voltage on the electrode makes the liquefied metal to form a sharp conical shape at the end of the needle. This is formed because of the electrostatic and the surface tension forces acting on the liquid metal. As the applied voltage is increased, the radius of curvature of the needle is decreased to such an extent that we have

ions being emitted from them. The radius of the apex (edge of the needle) is made approximately 5nm to obtain ions from it. A wide variety of metals like Al, As, B, Be, Bi, Cs, Cu, Ga, Ge, Fe, In, Li, Pb, P, Pd, Si, Sn, U, Zn are used as sources for FIB. One of the disadvantages of using a LIMS as source for a FIB system is that, we need to maintain the conical shape of the liquefied metal at all times. To maintain the conical shape, the force of interaction between the electric field, and the metal should be maintained at all times. This gives rise to internal stress in the metal because of replacement of source ions at the tip of the metal. The source ions are replaced by the flow of metal from the inside to the tip of the needle, which changes the stress from time to time. This is because the pressure of the internal liquid changes when the liquid metal flows to replace the depleted source. [13]

3.3 Beam Column

The beam column of a FIB system is shown in Figure 3.2. The beam column houses the source (LMIS), the extractor plates, and focusing section of a FIB system. The extractor plate helps in applying the high electric field near the source to extract the ions from the source. Once the ions are extracted from the source, it reaches the first pair of lenses. The lenses in the FIB system are electrostatic unlike the electron gun where it is magnetic. The electrostatic lens focuses the ions onto a beam steer/blanking plates, which is used for the sweeping or blanking the beam. The beam steer is used for removing small misalignment in the lenses, which causes defects in focusing. After passing through the beam steer/blanking plates, the ion beam passes through the drift tube and the stigmator plates. The stigmator plates help in exact positioning of the beam. Once the ion beam leaves the stigmator plates it passes through the deflector plates, which helps in positioning the beam at its final position. After passing through the deflector plates the beam passes through the second lens

arrangement, which then leads the beam to micro channel plate. Thus, with the help of these two lenses we will be able to achieve precision of up to 15 nm FWHM at 50 KeV with a current density of up to 5 A/ cm^2 [14]

3.4 Fabrication of silicon nitride membranes

As discussed, in Chapter 2 the design and fabrication of silicon nitride membranes are relatively simple when compared to silicon membranes. A detailed process flow, which describes the fabrication of silicon nitride membranes, is discussed in Appendix 1.Test membranes were fabricated using a mask made of rectangular patterns of different sizes as shown in Figure 3.3. There are two different sizes of squares and two different sizes of rectangles in the die, and their dimensions are given in the Table 3.1

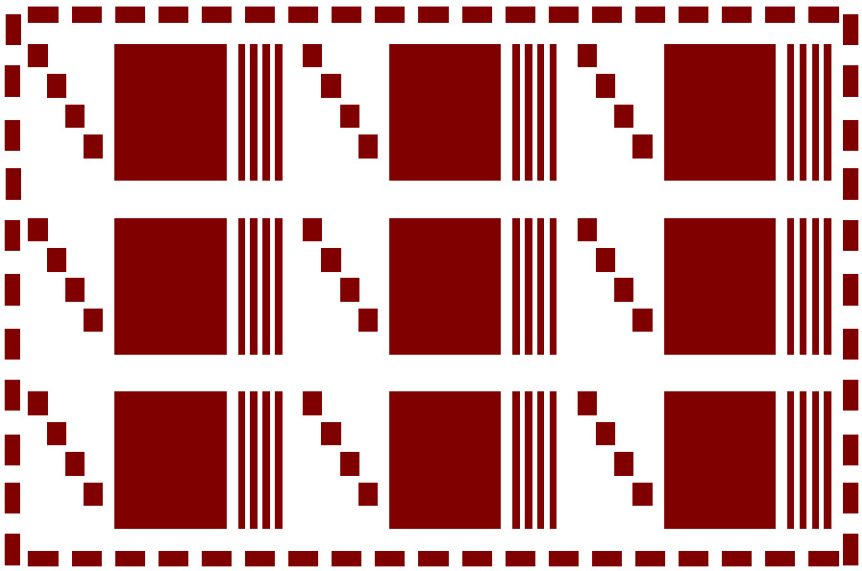

Figure 3.3. Die of the mask used for fabrication of test membranes.

Table 3.1. Dimension of features in the die

Feature description	**Feature dimension** μm
Large square	1500X1500
Small square	400X400
Large rectangle	1500X200
Small rectangle (die line)	500X300

All the test membranes were fabricated on a 250 μm thick, 100 dominant plane wafer. In order, to etch in the wafer in (100) plane we need to align the wafer to the $\langle 110 \rangle$ direction during patterning of silicon nitride. A faulty alignment will result in etching of other planes along with (100) plane. When silicon substrate is etched to get membranes at desired locations, the large, and the small squares, the substrate will also be etched in the other two features. The features on the mask which yields membranes, are the 2 squares which are of 1500 X 1500 μm^2 and 400 X 400 μm^2 in dimension. The larger square will result in a membrane area of approximately 1150 X 1150 μm^2, and the small square will yield a membrane area of 46 X 46 μm^2 area, in a 250 μm thick wafer. The cross section of the wafer is shown in Figure 3.4. The depth of the trench formed by the four features in the wafers is shown in the Table 3.2. It can be seen from Table 3.2, that the depth of etched trench depends on the smallest dimension of the feature.

Table 3.2. Depth of etched trench in the substrate

Dimension μm^2	**Depth of etched trench** μm
1500X200	141.23
500X300	211.85
400X400	282.47
1500X1500	1059.23

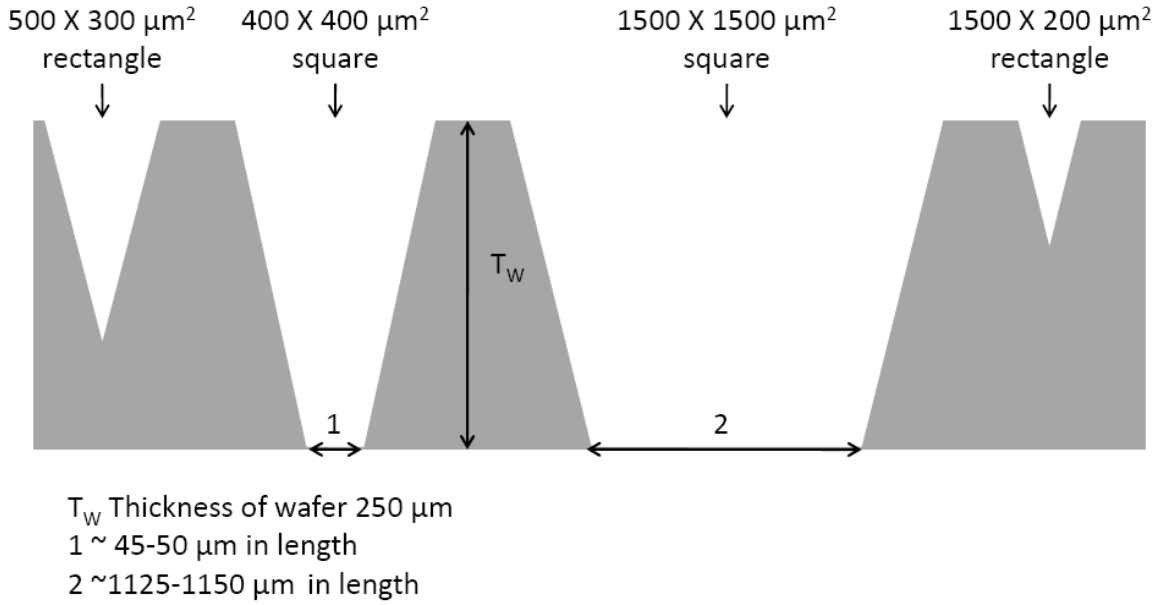

Figure 3.4. Cross-section of the etched silicon wafer (not to scale).

Though the wafer is etched in the other features, they do not result in a membrane because of their smaller dimensions. This however, still affects the mechanical stability of the wafer. Figure 3.5(a) through Figure 3.5(d) show the SEM images of the silicon wafer after etching in KOH. The process steps to be followed for fabrication of test membranes are depicted in Figure 3.6. Si_3N_4 was deposited using Low Pressure Chemical Vapor Deposition (LPCVD) technique at University of Texas at Dallas (UTD). The process was carried out at a temperature of 835^oC, with SiH_4, and NH_3 as the reactant gases. Figure 3.6 (a) depicts a 1-1.2 μm Si_3N_4 deposited on both sides of the wafer. The Si_3N_4 was then patterned and etched using Deep Reactive Ion Etching (DRIE) to from etch windows as shown in Figure 3.6(b) and 3.6(c). After, etching Si_3N_4, the silicon in the exposed regions were etched using 30 % KOH at 85 ^oC. The etch time was around 2-3 hours depending on the thickness of

the wafer. The cross-section of the wafer after etching is exhibited in Figure 3.6 (d). A detailed process flow for the fabrication of test membranes is given in Appendix 1.

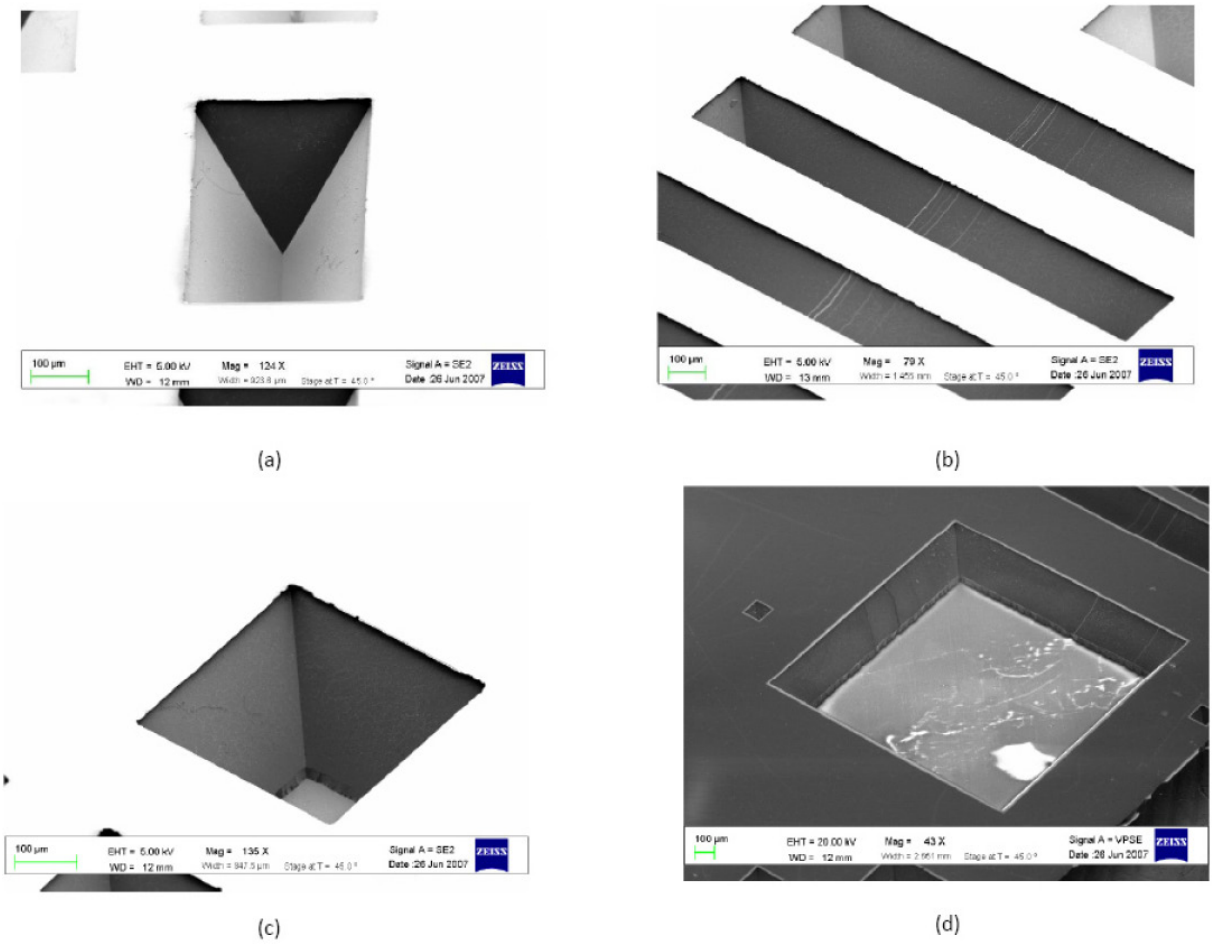

Figure 3.5. SEM images of different features in the die (a) 500x300 μm^2;(b) 1500x200 μm^2; (c) 400x400 μm^2; (d) 1500x1500 μm^2.

3.5 Pore design and fabrication

The pores on the membrane were drilled using FIB system coupled with NPGS. The CAD file, which was the input the NPGS system, consists of an array of dots

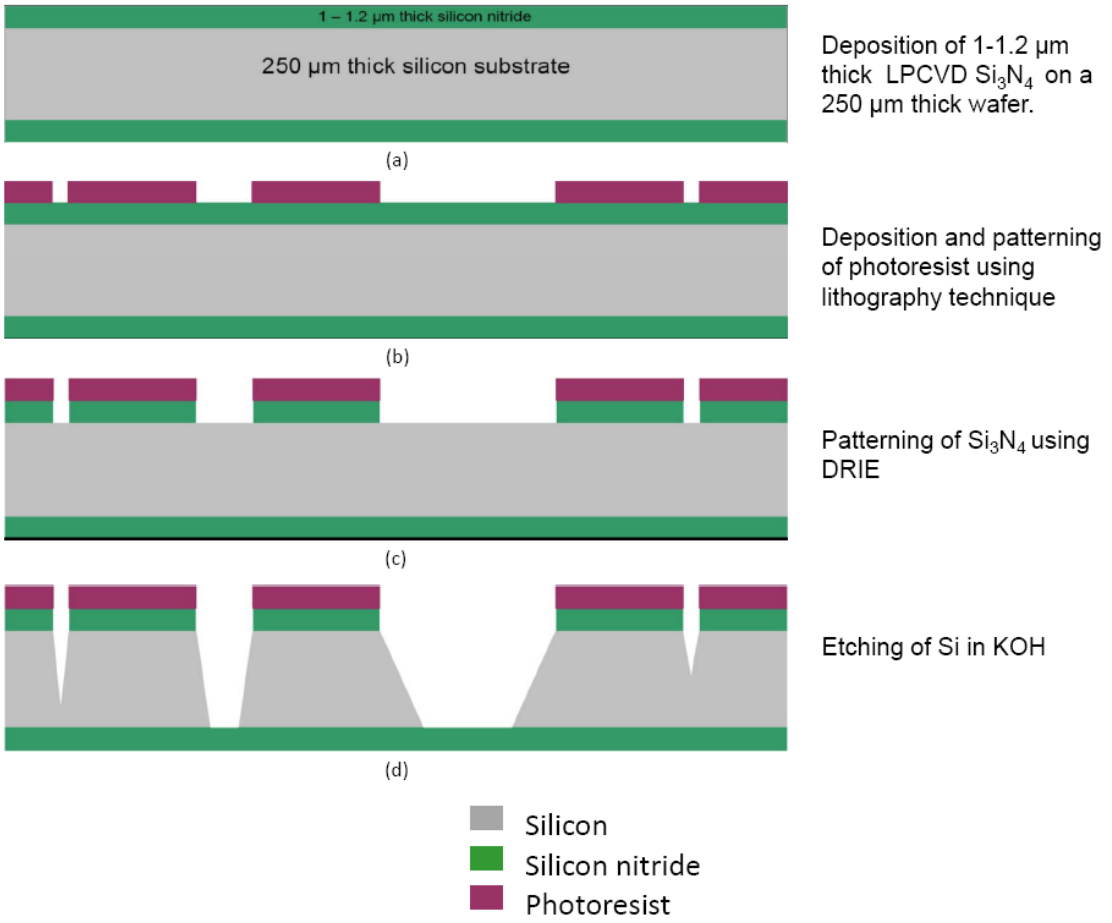

Figure 3.6. Steps for fabricating test membranes.

with different dimensions, which are transformed as pores on the membrane by the FIB system. The membrane was modeled for different porosities with different pore diameters. The porosity of the membrane was varied from 50 nm to 1500 nm with porosities ranging from 5 % to 40 %. The number of holes (N) for each porosity (P) depends on the area of the membrane (A_m), and area of a single pore (A_p)

$$N = \frac{A_m * P}{A_p} \tag{3.1}$$

Figure 3.7 shows the number of pores as a function of porosity. The membranes were sputtered with a very thin layer of gold. The thickness of gold was around 10

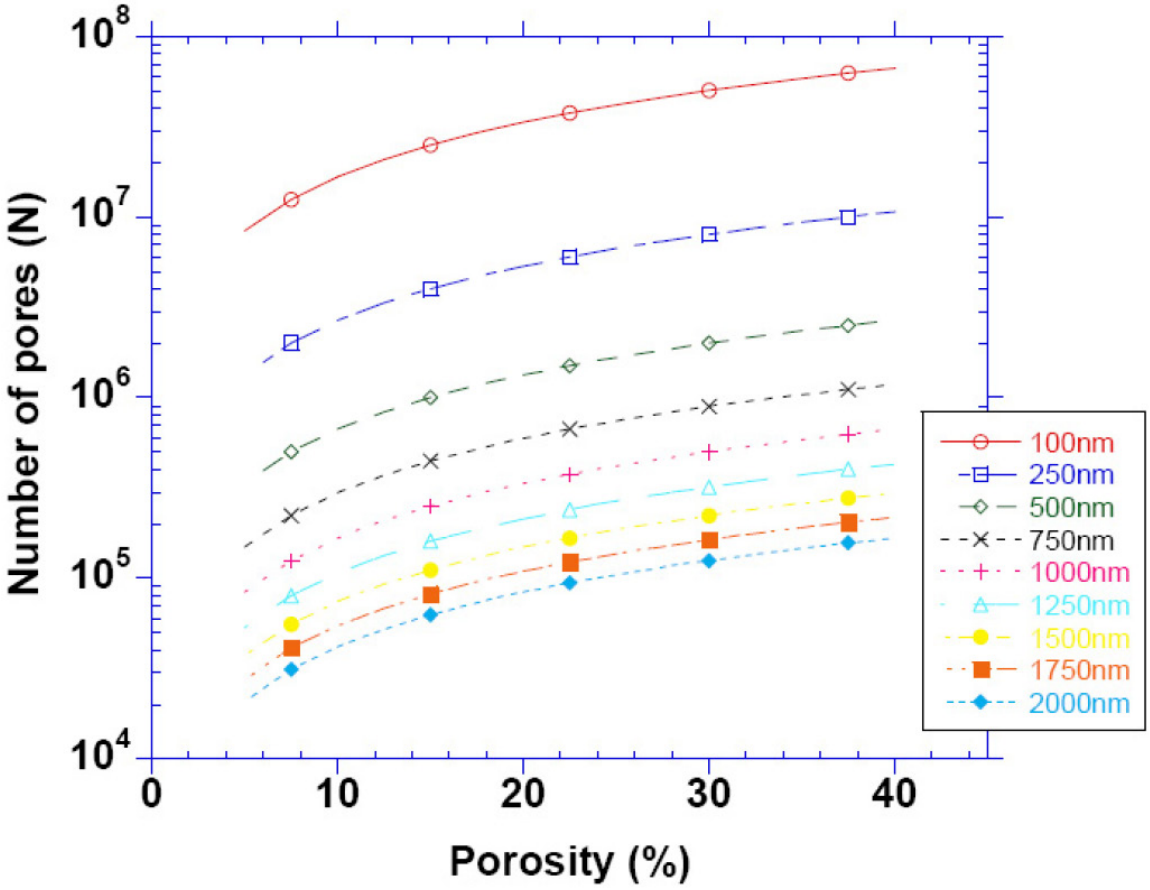

Figure 3.7. Number of pores and their corresponding porosities. Each curve represents a corresponding pore diameter.

nm. This was to reduce the charging effect caused by the Ga^+ ions when the pores are drilled. The fabricated membranes were placed inside the high vacuum chamber of the FIB system. After placing the sample carefully on the stage, the stage was hoisted to the required level of operation. The gun current was stabilized before the pattern of pores was fed to the computer, which controls the FIB. Controlling, FIB beam enables us to drill pores of specified porosity and dimension with precise placement of pores. This gives us complete control of the porosity for the whole membrane. The dimension of pores shown in Figure 3.8 is $4\mu m$ in diameter. Figure 3.9 clearly shows

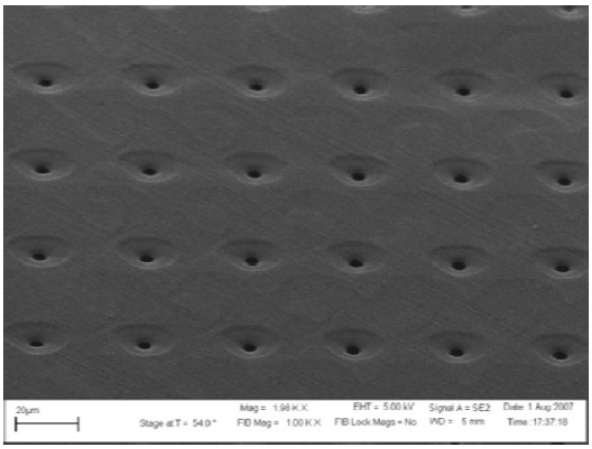

Figure 3.8. Pores of 4 μm diameter.

that the drilling of the pores has gone all through the membrane. If a closer look is taken at the pores on the right hand side of Figure 3.9, we are able to see the plane of silicon, which was made by etching of silicon. The pore on the left side of the image was made at a place where the silicon was not etched to form the membrane. Figure 3.8 is a SEM image of array of pores drilled on the membrane.

3.6 Mechanical testing of membranes

The fabricated silicon nitride membranes were tested for its stability, using a pressure sensor characterization setup. The setup has a probe tip, a load cell that is used to apply force on the membrane, a weigh scale to measure the applied weight in grams, and a computer to control the movement of the probe. The arrangement for the pressure sensor characterization setup is shown in Figures 3.10 and 3.11.

The load cell has a resolution of 1 milligram. The load cell can apply a maximum load of 10 grams in weight. The sample was placed in the stage, and the probe was moved down on the membrane in steps of 2 μm up to 50 μm. The diameter of the probe was assumed to be 500 μm. Using the diameter of the probe, the pressure

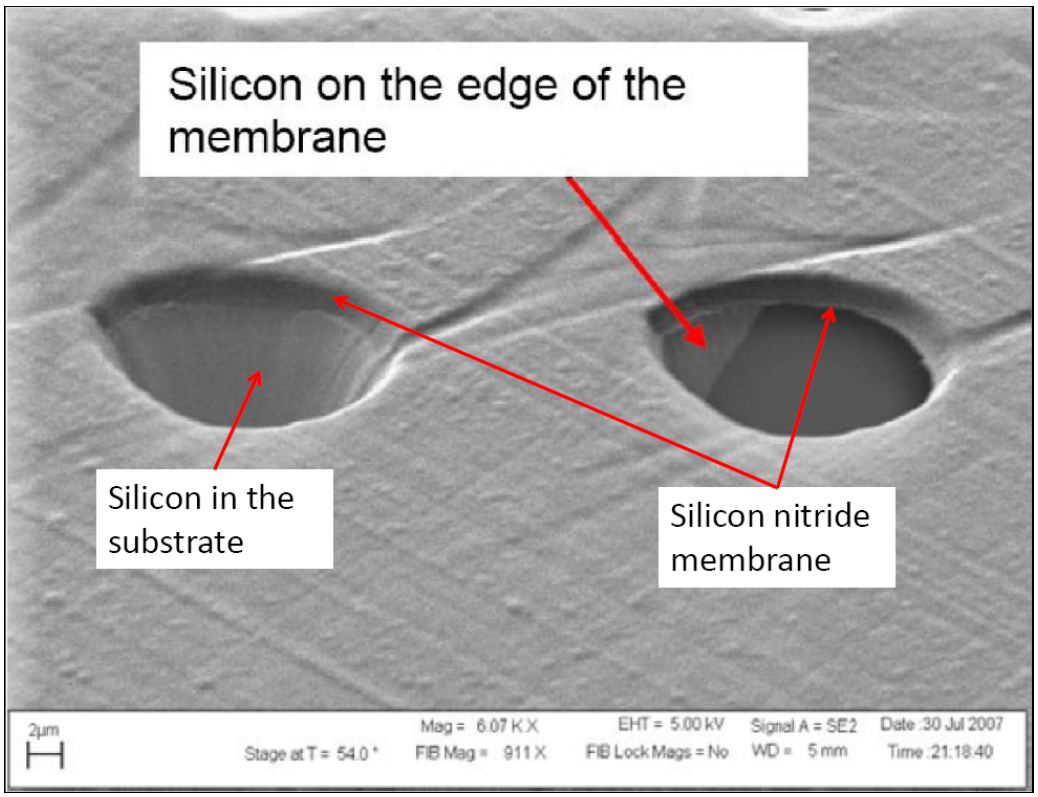

Figure 3.9. Pore on the edge of the silicon membrane.

exerted on the membrane by the probe was calculated. The non-porous membranes were subjected to pressures ranging from 500 Pa to 2.12x10^5 Pa. There was no visible deformation or damage on the membrane because of the applied load. This verifies that the membrane can be subjected to high pressures without any appreciable damage to the membrane. Figure 3.12 shows the displacement of the non-porous membrane for the applied load.

Table 3.3 details the different porous membranes fabricated using FIB. Table 3.3 gives us the number of pores on the membrane with its dimensions, and lists the pressure exerted by the membranes for a displacement of 2 μm and 50 μm. The non-porous membrane showed a higher pressure exerted, for the same displacement. Though the non-porous membrane showed a higher pressure, there was no visible

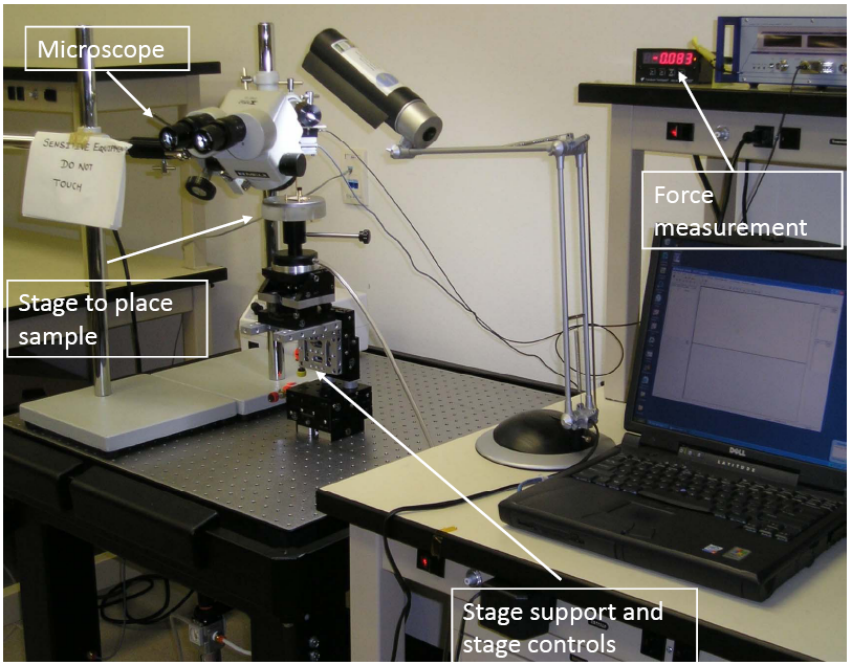

Figure 3.10. Pressure sensor characterization setup.

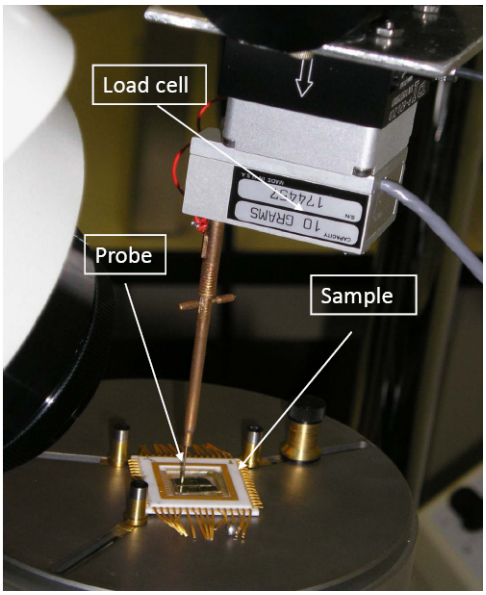

Figure 3.11. Pressure sensor characterization setup 2.

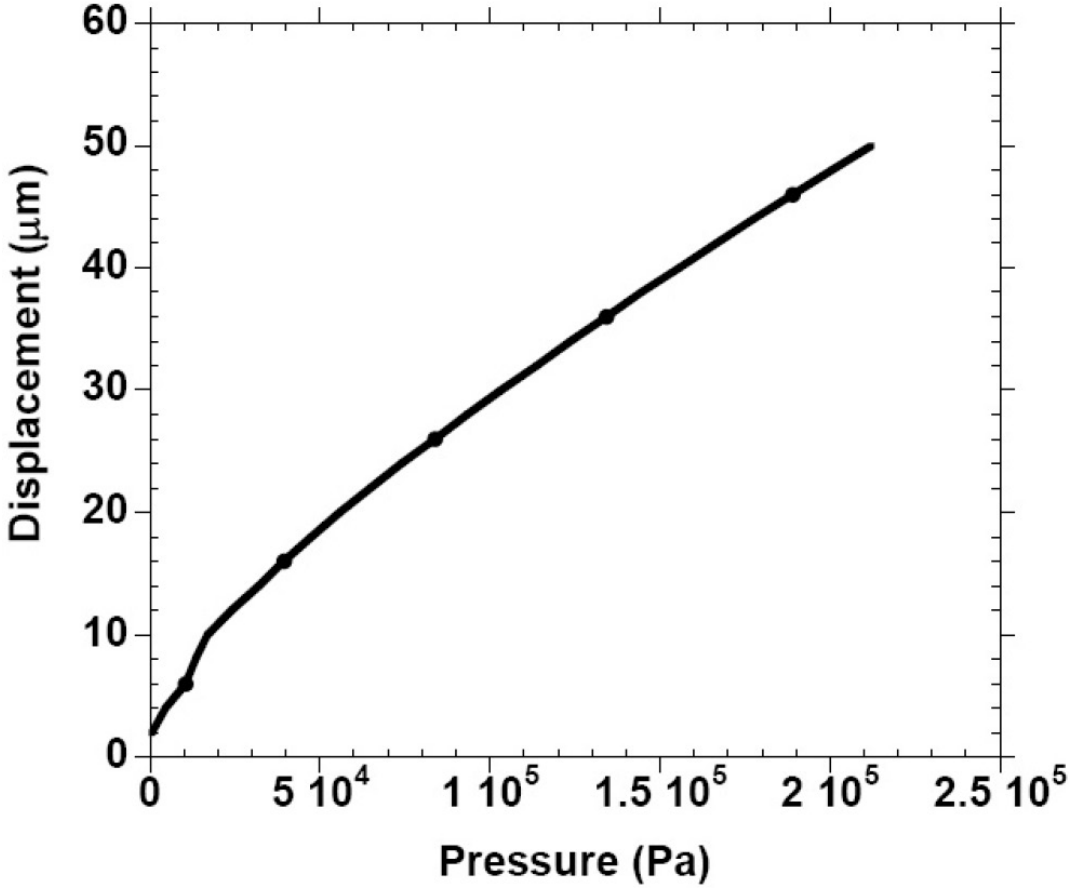

Figure 3.12. Displacement of non-porous membrane with respect to applied pressure.

damage to the membrane. The pressure exerted on the membrane for the same displacement was found to be relatively similar to the non-porous membrane with increase in the porosity of the membrane. This can be attributed to the high yield strength of silicon nitride, which is of the order of 304 GPa. Figure 3.13 shows the comparison of the variation of pressure corresponding to displacement for both porous and non-porous membranes.

Table 3.3. Different membranes fabricated using FIB and their mechanical stability results

Name	**Porosity (%)**	**Number of pores-pore dimension (μm)**	**Pressure calculated for 2 μm displacement (MPa)**	**Pressure calculated for 50 μm displacement (MPa)**
MEM1-0%	0%	N/A	0.005	0.21
MEM1-0.1% -4.45	0.1%	104-4.45	0.0026	0.1202
MEM1-0.2% -8	0.19%	52-8	0.0042	0.1711
MEM1-0.2%-4.3,4.6,1.8	0.21%	100-4.3, 80-4.6, 80-1.8	0.0006	0.1158
MEM1-0.5% -6.236	0.54%	225-6.236		
MEM1-1% -10.34	0.95%	160-10.34		

3.6.1 Simulation of mechanical testing

The membranes were simulated for mechanical stability, before experimentally testing the membranes. The experimental setup was recreated in a virtual environment using Coventorware. The software create a 3-D models for the nanoporous membrane and uses finite element (FEM) to analyze different properties such as mechanical strength, thermal conductivity, microfluidic properties etc. depending on the module used. The simulation results obtained on different porous membranes with uniform porosity are discussed in this section. In the experiment, a 500 μm diameter probe tip was used. In order to emulate this, a patch of 500 μm diameter was created on the membrane surface, and a uniform pressure was applied on that patch. A 3-D model of the structure was created corresponding to each porosity from the process flow and layout using Coventorware. For the simulation purposes, only the membrane

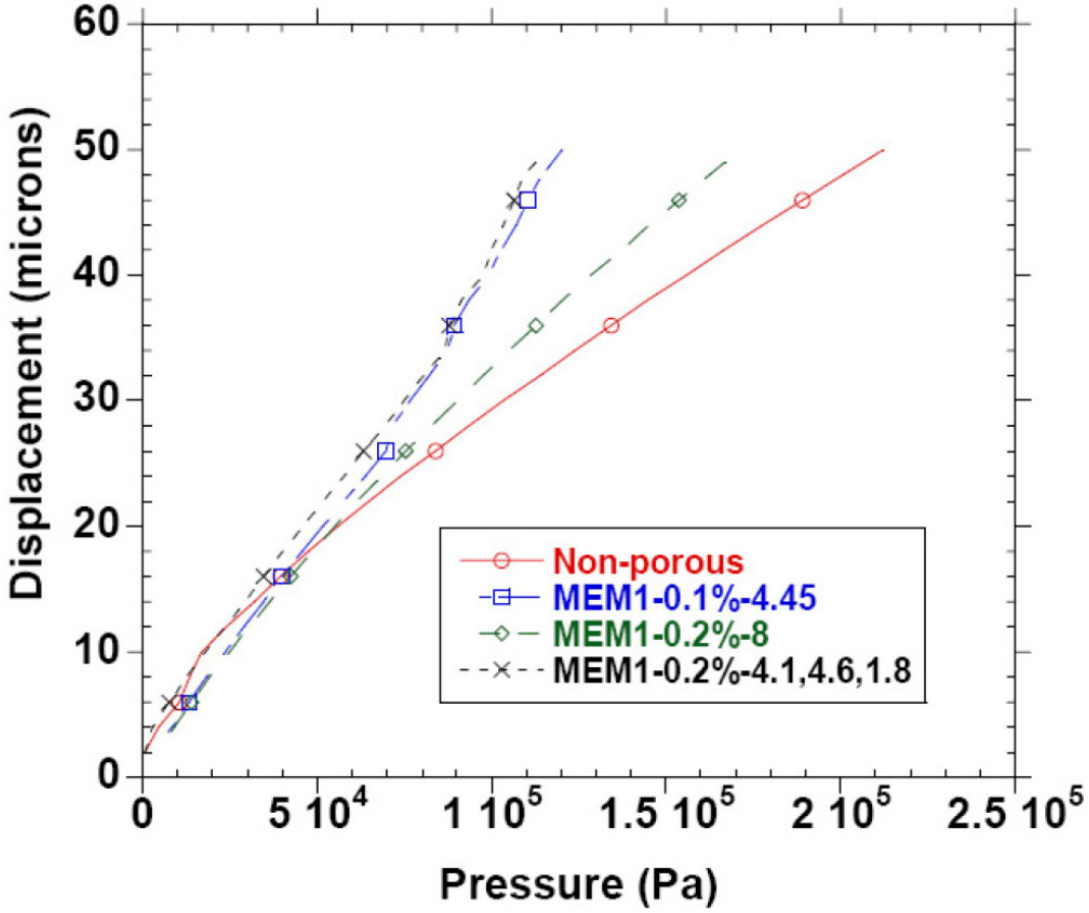

Figure 3.13. Comparison of porous and non-porous membrane displacement for applied pressure.

layer of the silicon nitride was used. The mesh element was chosen as extruded bricks with parabolic elements, due to higher number of points at which the membrane is probed. For all our simulation runs, we employed the four-fold symmetry of the rectangular membrane. This allows us to use only quarter of the membrane, which saves time. Figure 3.14 shows the meshed structure along with the boundary conditions.

The module, which was used for simulating the mechanical stability, was MEMS mechanical or MEMMECH. The material used in simulation was assumed elastic, and linear in nature. The two sides of the membrane were fixed, a uniform load of 0 MPa

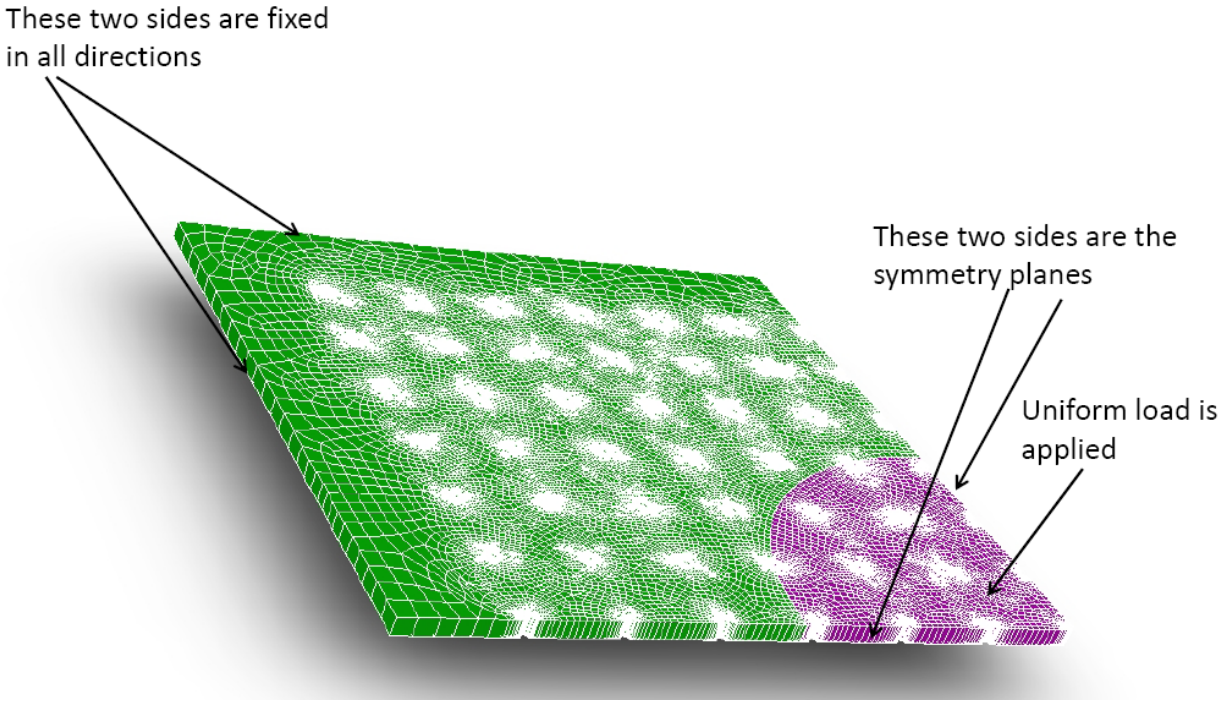

Figure 3.14. Boundary conditions applied to the simulated membrane.

Table 3.4. Material properties used for simulation of membrane

Material	**Young's modulus** GPa	**Poisson's ratio**
Silicon nitride	304	0.24

Table 3.5. Simulation results for application of 0.25 MPa

Porosity %	**Displacement with 0.25 MPa pressure (μm)**	**Von Mises stress MPa**
0.2	25.69	862.003
0.4	25.73	835.006
0.6	25.76	886.099
0.8	25.82	1395.545

to 0.25 MPa was applied on top surface in steps of 0.05 MPa. These values correspond to 0 cm to 2550 cm of water pressure, respectively. 0.04 MPa (450 cm of water) is the maximum pressure, which is to be experienced by the membrane during normal operation. Young's modulus and Poisson's ratio values entered into the software material database are listed in Table 3.4. The silicon nitride membrane was allowed to move only in the z-direction, by applying boundary conditions to fix the edges of the membrane in all directions, and allowing the membrane to displace in the negative z-direction. The observed values for maximum displacement and Von Mises stress for each design is tabulated in Table 3.5.

3.7 Comparison of simulation and experimental study

In order to check the consistency between the simulation and experiments, we compared the results obtained for the 0.2% porous membrane. As seen in Figure 3.15, the applied pressure of 0.05 MPa, the simulation and experimental results agree with each other within experimental error. Since the range of pressure that the membrane will be subjected during typical use is even less than this value, we are confident that the membrane's mechanical strength is established both experimentally and theoretically. The introduction of pores has increased the displacement of the membrane for the same applied pressure but the displacement was not much deviant from the non-porous membranes.

For higher values of pressure, 0.15 MPa to 0.2 MPa, the porous membranes show a displacement values close to 50 microns. The simulation results for the mechanical study of the membrane resulted in a considerably less displacement for the same pressure range. This could be because of the following reasons:

- The calculation of the pressure exerted on the membrane was done assuming that the probe tip has a diameter of 500 μm. In reality, the part of the probe,

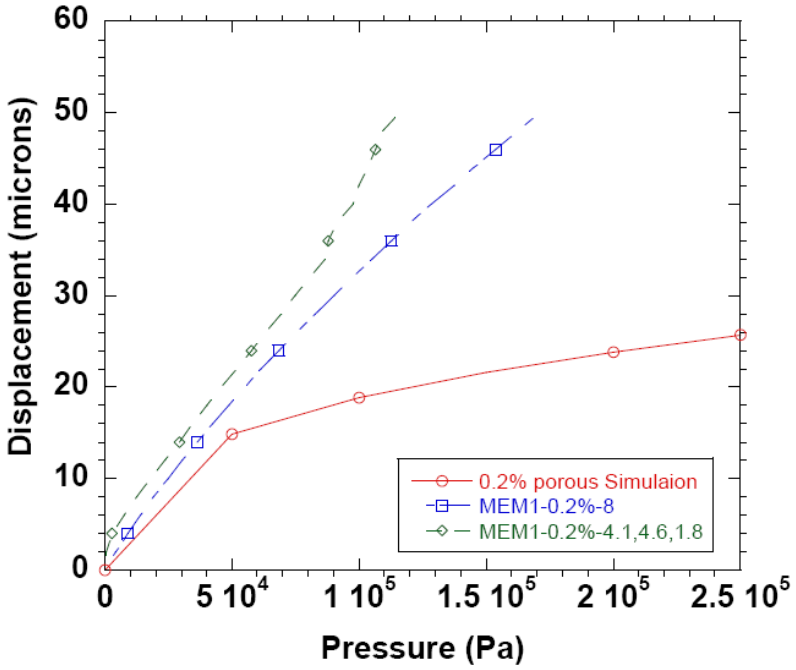

Figure 3.15. Comparison of simulation results and experimental values for 0.2% porous membrane.

which is in contact with the membrane, has a smaller diameter. Since the area, which is in contact with the membrane is less, the pressure exerted on the membrane is higher than calculated. This could be one of the reasons for the difference in results obtained from simulation and testing.

- The simulation assumes that there is uniform pressure throughout the circular patch defined on the membrane. In reality, this will not be the situation, as the membrane will wrap around the tip of the probe thus displacing farther. This effect would be more prominent at higher applied pressures, thus, making the discrepancy between the experiment and the simulations more pronounced.

3.8 Oxygen permeation study of porous membranes

The porous membranes were studied for oxygen permeation using Illinois Instruments Oxygen Permeation Device Model Number 8001,which measures the oxygen transmission rate across a membrane based on the concentration difference. A schematic diagram of the test chamber is shown in Figure 3.16. The test membrane is mounted to a window that separates two gas channels. Oxygen is allowed to flow through the upper channel and nitrogen is allowed to flow through the lower channel. Gas flows are regulated such that two channels have the same flow rates with zero convective pressure across the membrane. Oxygen molecules diffuse through the membrane because of concentration differences. Oxygen transmission rate (OTR) is a permeability measure for the amount of oxygen that diffuses across the membrane per unit time, per unit area.

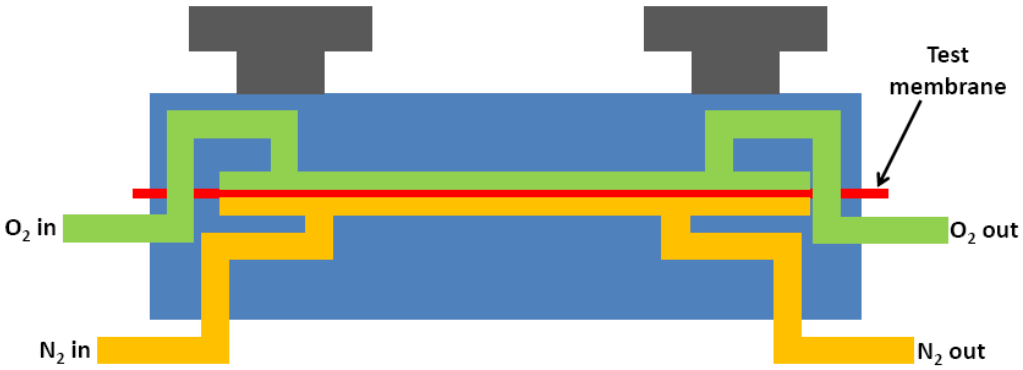

Figure 3.16. Cross-section of oxygen transmission rate test chamber.

The porous membranes were mounted on the steel plate such that the membrane with the pores is placed at the center of the opening in the steel plate. A self-adhering masking foil was used to place the sample at the fixed position during the test. A sensor at the lower channel detects the amount of oxygen molecules and registers it to

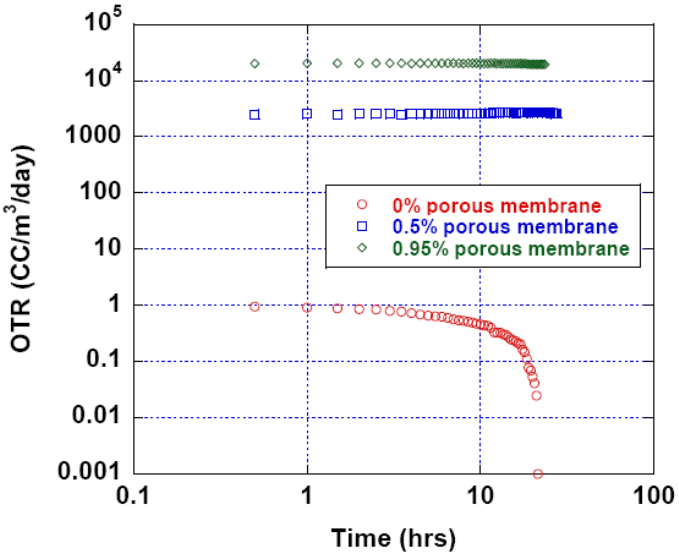

Figure 3.17. Variation of oxygen transmission rate with respect to time.

a connected PC at a specified sampling rate. Extra caution is needed when applying masking foil to eliminate any possible gas leak due to trapped air pockets. Grease was also applied to the outer edge of the wafer in an effort to eliminate any air pockets.

The results of our preliminary testing is shown in Figure 3.17. As expected, the 0% porous membrane was impermeable as the OTR was recorded a negative value after approximately 55 hours of testing. The OTR results of 0.5% and 0.95% are also shown in Figure 3.17. The ORT for 0.5% was stablized at 2570 $cc/m^3/day$ and the ORT of 0.95% was found to be 19276 $cc/m^3/day$. Although these results are preliminary, they show that the porous membranes allows sufficient transfer of oxygen from one side of the membrane to the other side. (OTR study was done with help of Prof. C. Chuong and S. Uttamaraj of BME department).

3.9 Summary

This chapter discussed the fabrication of porous test membranes using a FIB system. Membranes with varying porosities were tested for their mechanical stability using a pressure sensor characterization setup. The porous membranes were also simulated for their mechanical stability using Coventorware. The results obtained from simulation, and the experiment were compared, and a good agreement was obtained for the pressure values relevant to our application. In Chapter 4 we discuss the fabrication of nanopores using nanoimprint lithography.

CHAPTER 4

NANOIMPRINT LITHOGRAPHY

4.1 What is Nanoimprint lithography?

Lithography is a technique used to transform images carved on stone to any smooth surface or to a paper. Lithograph is a pattern formed using the process of lithography where the carved stone is painted with ink, and the carvings on the stone are transformed to the paper or the surface. This was first developed by Bavarian author Alois Senefelder in 1796 [15]. Since then the technique has evolved, and has helped in fabrication techniques of integrated circuits and MEMS devices. The same principle as used in lithography is applied to photolithography, where light in the form of ultraviolet (UV) is used to make the required patterns. The major drawback of using optical lithography is the wavelength of the employed light, and the interference caused by the reflected radiation from the substrate, which restrict the feature dimensions that can be fabricated using photolithography technique. This led to the development of other techniques, one of which is the nanoimprint technology, thus enabling features of the scale of 10 - 50 nm. Nanoimprint lithography (NIL) can be broadly defined as patterning of a soft polymer using a hard mask. By employing NIL technology, we will be able to pattern devices with less than 10 nm line width. For our fabrication, we concentrated on thermal imprint lithography where we used elevated temperatures to transfer the pattern from the mold to the polymer. The other ways to assist transfer of pattern are

1. UV-NIL: In this type of imprinting, UV-light is used for transfer of pattern form the mold to the resist. The mold used in UV-NIL is transparent to UV light,

usually made of quartz. Since there is no heating involved, this process is much faster than thermal NIL. UV-NIL is mainly used for step and repeat imprint technique. The drawback of using this process for step and repeat imprint is that the features already imprinted are affected by later imprinting [16].

2. Laser assisted imprinting: There are two types of laser assisted imprinting; Laser Direct Imprinting (LDI) and Laser Assisted Imprinting (LAI). In LDI, XeCl excimer laser is used to melt the silicon substrate. The mold used in this type of imprinting needs to be transparent to laser, and is generally made of quartz. During the imprint process the laser is pulsed to melt the substrate, which under pressurized condition takes the shape of the features on the mold upon cooling. LAI is very similar to LDI except, in LAI a polymer is melted using the laser instead of the Si substrate [16].
3. Self-assembly NIL: In this NIL, there is no actual contact between the mold and the polymer. The mold is placed 100 nm on top of the polymer. When the temperature of the arrangement is increased during the imprint cycle, there are pillars which grow on the polymer and take the shape of the mold. The limitation of this type of imprinting is that we will not be able to imprint high aspect ratio features in the polymer [16].
4. Contact inking: Contact inking is an indirect imprinting technique. In this NIL a silicone substrate is patterned using a silicon mold. The patterned silicone substrate is then chemically treated with the required chemicals, and used a mold for patterning. When brought into intimate contact with the treated surface of the substrate, the substrate absorbs the chemicals from the mold, thus transferring the features from mold to substrate. This technique is usually used for formation of self-assembled monolayer (SAM) and to make masks for gold etching [16].

4.2 Thermal nanoimprint lithography (NIL)

Thermal nanoimprint lithography (NIL) like any other imprinting technique uses a hard mask, generally made of silicon to transfer the patterns to the resist. The hard mask is pressed on the thermal imprint resist under temperatures greater than the glass transition temperature of the resist. Glass transition temperature in simple terms can be defined as the temperature below which the material becomes brittle, and above which the material becomes soft. This property of the material is used in thermal imprint lithography. The working of a NIL can be presented in the following two steps

1. The substrate with thermal imprint resist is heated above the glass transition temperature of the thermal imprint resist.
2. The mold is pressed on the heated substrate to transfer the pattern from the mold to the substrate. The mold and the substrate are cooled down to complete the pattern transfer.

After the application of pressure on top of the mold for the stipulated time, the mold and the substrate are cooled together to room temperature. This allows the imprint resist to become a brittle material with the pattern transferred from the mold. Figure 4.1 shows the process description of a NIL. The stamp and the mold are brought in contact with each other. When the temperature of the sample exceeds the glass transition temperature of the polymer film making it a viscous liquid, pressure is applied on the mold as depicted in Figure 4.1(b). The pressure is maintained for a stipulated period. The temperature of the sample is brought well below the glass transition temperature before the mold is separated from substrate. Once the sample is brought below the glass transition temperature the polymer film solidifies, and the pattern on the mold is transferred to the polymer film. The patterned polymer film

is dry etched to transfer the features to the substrate. This is depicted in Figure 4.1(d) [17].

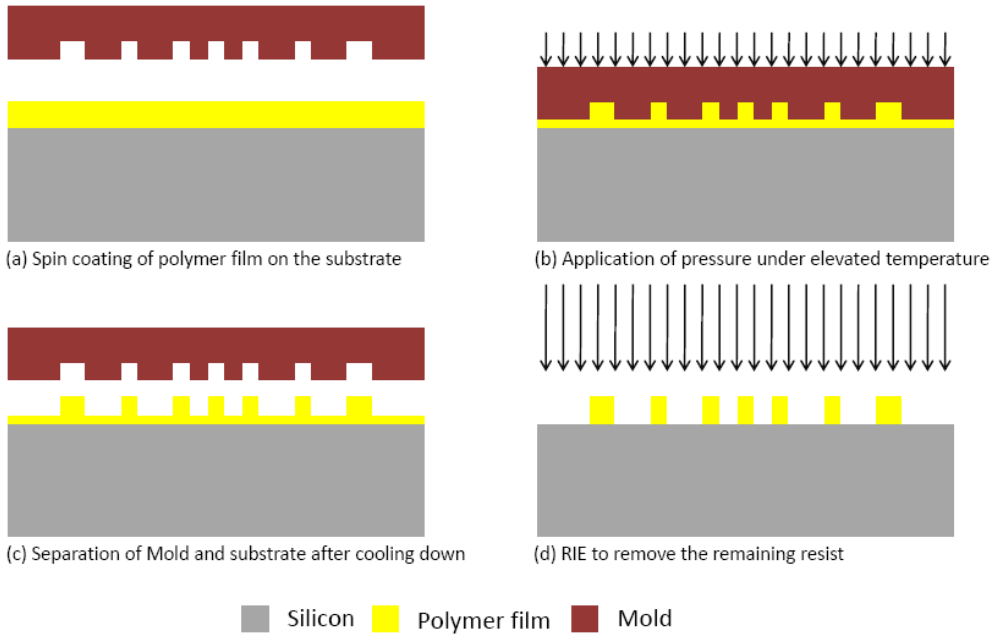

Figure 4.1. Process flow of thermal nanoimprint lithography.

4.3 Types of nanoimprint lithography

There are three types of nanoimprint lithography techniques; single-imprint, step and repeat, and roller machines. In a single-imprint technique, the whole wafer is imprinted at the same time. In order to achieve this we require a mold, which is of the same size of the wafer or of a smaller dimension than the wafer with features at the required regions. The processing of the single-imprint machine is very similar to the process described in Figure 4.1. Single imprint technique can be either UV-NIL or thermal NIL.

The step and repeat imprinting technology is very similar to step and repeat optical lithography. In this technique, a mold smaller in dimension than the wafer is used. The mold is imprinted at the first point as in single-imprint technique, and is moved to a fixed distance in the x and y direction to repeat the process. In this way, the entire wafer can be covered using a small mold. The main advantage of this method over single-imprint method is, the size of the mold used in step and repeat is much smaller than the size of the substrate, thus reducing the cost of fabrication of the mold. Figure 4.2 shows the operation of a step and repeat imprint process. Figure 4.3 b and Figure 4.2 d shows the cross-section of the wafer across X and X‘ [17].

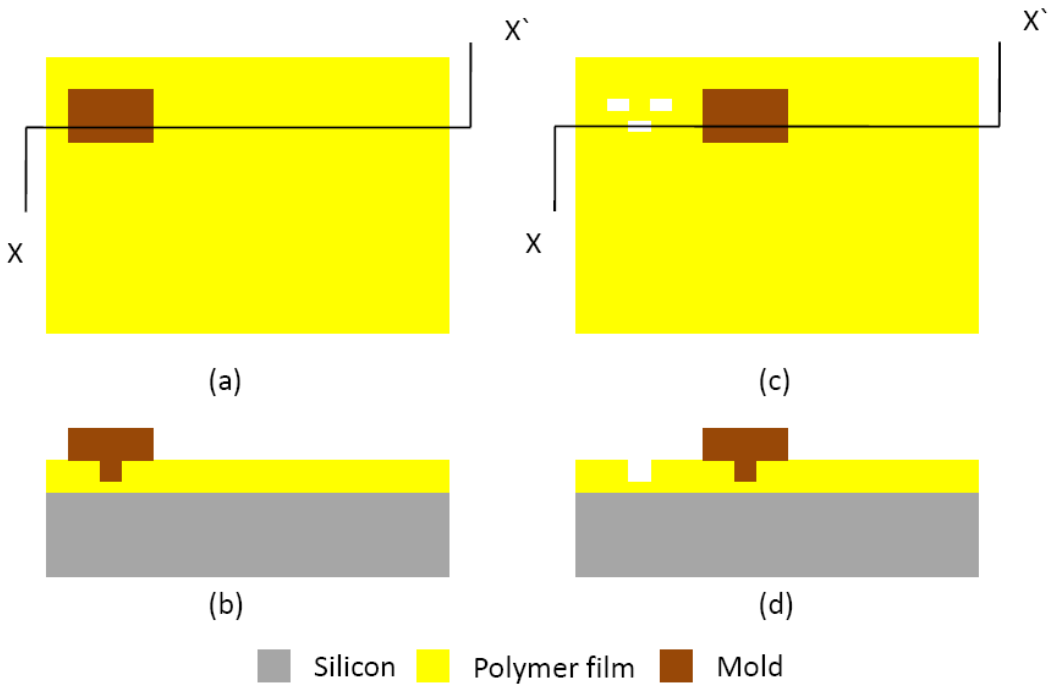

Figure 4.2. (a & c) Top view of the substrate during first and second imprint;(b & d) Cross-section of the wafer during first and second imprint.

The other type of imprinting technique is that of roller imprinting where a roller is employed to apply pressure on the mold. There are two different types of roller imprinting namely roller imprint and cylindrical roller. In roller imprint, the mold used for imprinting is very similar to the ones used in single-imprint and step and repeat techniques. The application of pressure in the roller imprint technique is done using a cylinder, which is rolled over the mold when in contact with the polymer at a temperature greater than the glass transition temperature of the polymer. In the cylindrical roller technique, the mold is wrapped around the cylinder, which is used to press the mold against the polymer. In order to ensure accurate transfer of features from the mold to the polymer, the polymer is operated at a temperature lower than the glass transition temperature, and the mold is heated above the glass transition temperature of the polymer. Figure 4.3 a shows the roller imprint technique, and Figure 4.3 b shows the cylindrical mold technique [17].

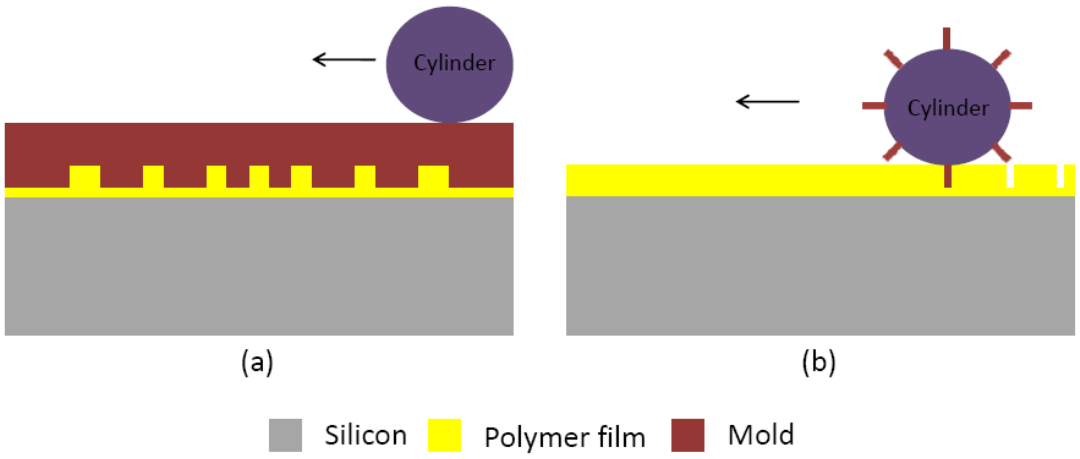

Figure 4.3. (a) Flat mold with cylindrical roller on top; (b) Cylindrical mold roller imprint technique.

4.4 Mold Fabrication

The mold for imprinting was made using e-beam lithography, and successive RIE etching. There are two types of molds that can be fabricated namely; silicon mold and metal-on-silicon mold. The Si-based mold involves the use of e-beam lithography and RIE etching techniques. The metal-based mold employs e-beam lithography process followed by metal deposition, and lift-off of the deposited metal. The two types of molds mentioned above are easy to fabricate when the area of the die is small, and the features are sparsely located on the die area. However, the fabrication becomes much more complex, when the density of the features in the mold area increases or if there is an increase in mold dimension. In such cases, techniques such as holography or interference lithography are employed to create the mold.

We fabricated a Si mold with holes of 160 nm in diameter and with a pitch of 500 nm. In order to fabricate stamps on silicon substrate ZEP-520, a positive e-beam resist was used. The resist was 300 nm thick after spinning at 2600 rpm and curing at 180^{o}C. The resist was exposed using electron beam with an area dose of 100 $/cm^2$. Following the exposure of the resist in e-beam to obtain the required pattern, the resist was developed for 1 minute in ZED N-50, rinsed with ZPA for 5 minutes, and was inspected under the microscope for uniformity. The next step in preparation of silicon-based stamp is etching of the substrate to form the pattern in RIE. The stamp was etched for 300 nm depth in the patterned regions in a chlorine environment a mixture if Cl_2 and BCl_3.The etch selectivity of the resist to silicon in this composition is 2:3. Figure 4.4 depicts the process flow for the fabrication of silicon-based stamps. Figure 4.5 shows a SEM image of the Si based stamp.

The mold that was used to fabricate pores on the membrane had pillars of diameter ranging from 150 nm to 250 nm. The pitch of the pillars on the mold is 500 nm. This mold was purchased from NIL technologies, Denmark. The pattern on

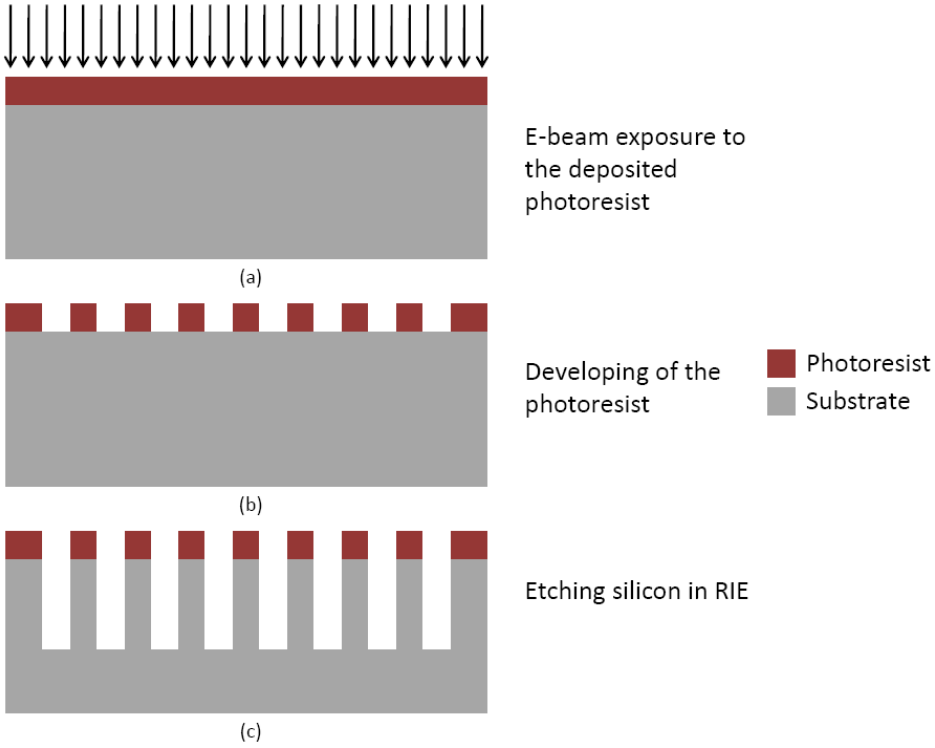

Figure 4.4. Fabrication of Silicon mold.

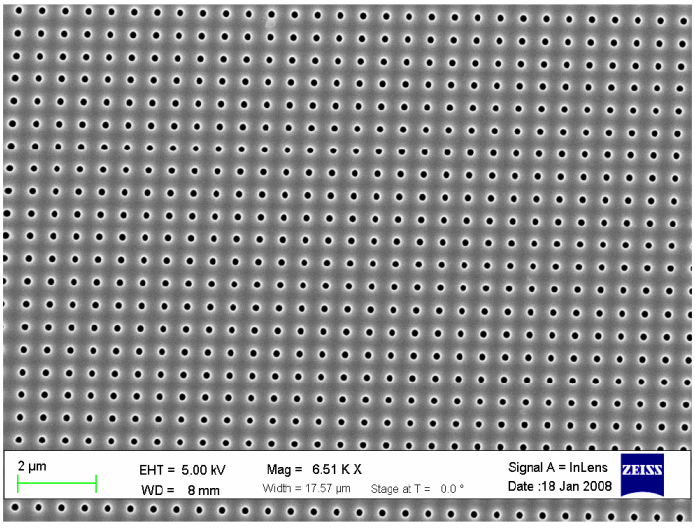

Figure 4.5. Holes of 300 nm depth on silicon. The diameter of the holes is 160 nm and the pitch is 500 nm..

the outside 3 mm of the mold did not have proper features because of handling effect and due to the edge effect when the resist is spin coated. The height of the pillar is 120 nm with a variation of 5% in the height of the pillar. The mold was coated with 1H,1H,2H,2H-perflourodecyltrichlorosilane ($C_{10}H_4Cl_3F_{17}Si$) as the anti-stiction layer. Figure 4.6 (a) shows the SEM image of the mold and Figure 4.6 (b) shows the results of the AFM analysis on the mold. The images shown in Figure 4.6 (a) and (b) are courtesy of NIL technologies, Denmark.

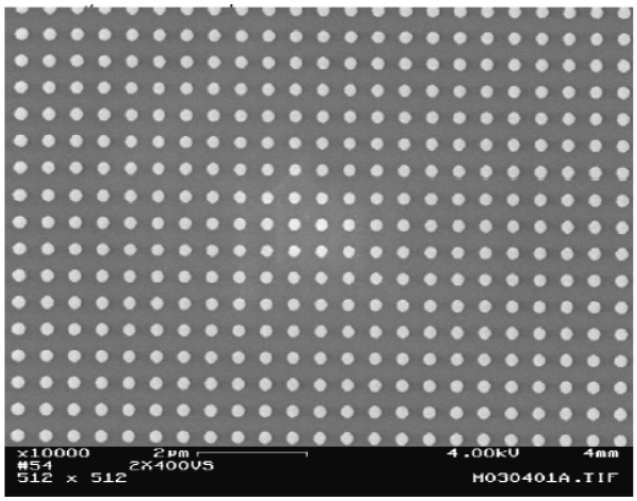

(a) SEM analysis of the mold

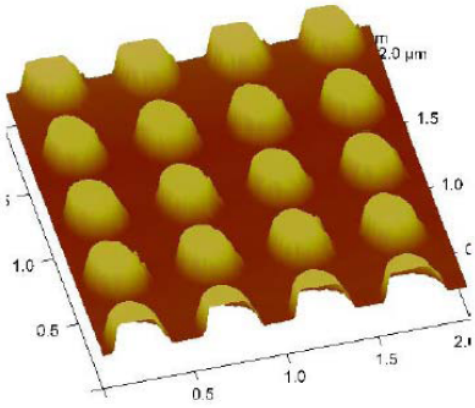

(b) AFM analysis of the mold

Figure 4.6. SEM and AFM analysis of the mold, Courtesy NIL technologies, Denmark.

4.5 Anti-stiction coating

During imprinting, the mold and the imprint resist come into close contact with each other. If the surface energy of interaction between imprint resist and the mold is greater than the surface energy of interaction between the substrate and the resist, there are chances that the resist might adhere to the mold either at parts or through

the entire wafer. This will result in poor imprint or no imprint. In order to counter the effects of the resist sticking to the mold, the mold is coated with a very thin layer of an anti-stiction layer, which can be attached to the surface of the mold physically or chemically. The thickness of the anti-stiction layer is no more than 5 nm as it might affect the features on the mold. Generally, the anti-stiction layer is attached chemically on to the wafer surface. The wafer surface is cleaned thoroughly using piranha solution to remove any dirt on top of the wafer. Piranha solution which was used for our purpose was a base piranha which is a mixture of NH_4OH and H_2O_2 in 3:1 ratio. The solution was heated to 85 ^oC before immersing the mold to remove dirt and organic materials. Subsequently, the wafer is immersed in the solution containing the mixture of the anti-stiction layer for the required time. The mold is then rinsed with DI-water and is blow-dried. Figure 4.6 depicts the coating of anti-stiction layer on top of the mold.

4.6 Imprinting

Nanonex NXB-200 imprinter was used for imprinting, which allows imprinting of the entire wafer at once. The maximum dimension of the wafer, which can be imprinted, is 3 inch in diameter. The resolution on the equipment is less than 10 nm. The equipment is optimized for replication of small structures on Si, GaAs, metal and ceramic substrates.

Nanonex NXB-200 has the capability to process both thermal and UV based NIL. The imprinter houses a UV source which performs UV based NIL. In order to perform thermal NIL, the equipment has a heater, which can operate with a wide range of temperatures, which makes it possible for the equipment to operate with a wide range of thermoplastics. The process parameters for our imprinting are listed in Table 4.1. The total time required to complete the process is approximately 3

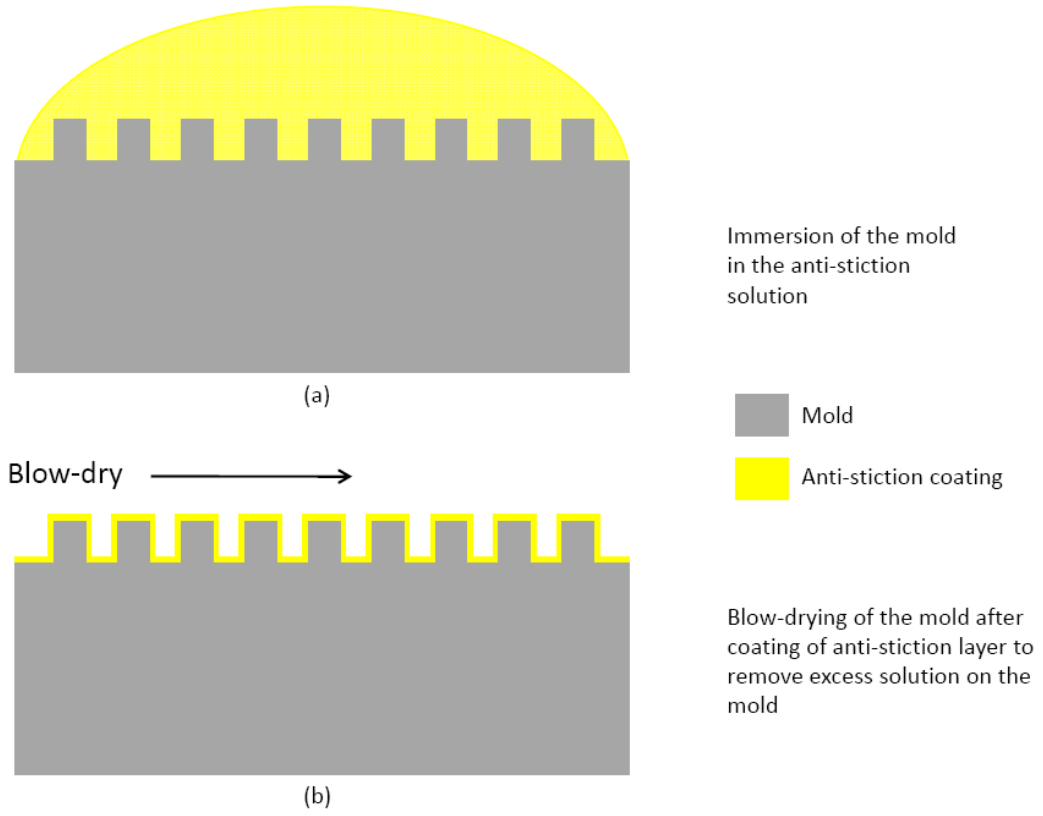

Figure 4.7. Deposition of anti-stiction layer coating.

minutes. The pressure applied for our process is 200 PSI with a preimprint pressure of 120 PSI. The process temperature is set to 130 ^oC, which is above the glass transition temperature of NXR-1020, the polymer used. The applied pressure is uniform throughout the sample, which helps in reducing the errors in the imprinting caused by the surface variation defects on the wafer. The chamber in which the wafer is placed along with the mold is shown in Figure 4.8.

The chamber that houses the mold and the substrate has two circular plastic sheets to keep the mold and the substrate in position during imprinting. The diameter of the bottom plastic sheet is bigger than the top plastic sheet. The chamber also has a thermocouple, which helps in monitoring the temperature of the sample during

Table 4.1. Process parameters for nanoimprinting

Parameter	Values
Initial pressure	120 PSI
Operation pressure	200 PSI
Operation temperature	130 ^oC
Operation time	30 sec

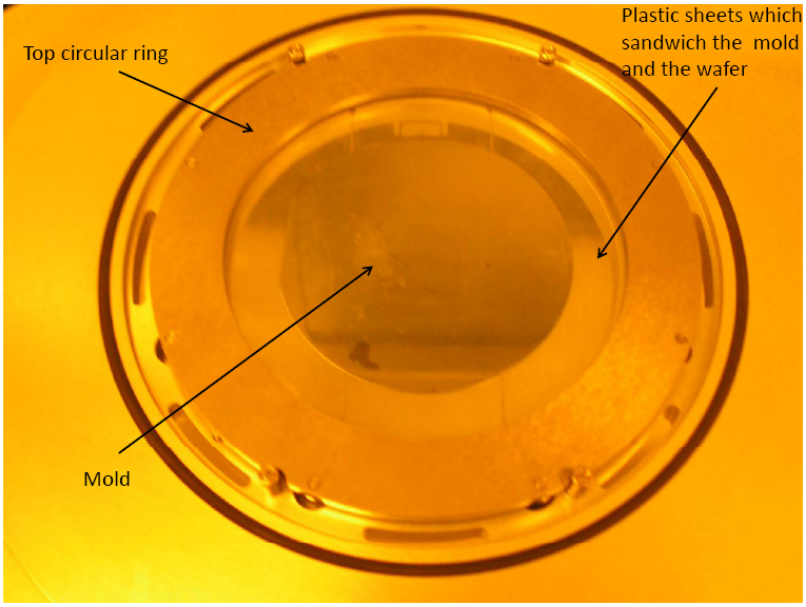

Figure 4.8. Mold inside the imprinting chamber.

imprinting. After placing the substrate and the mold between the two plastic sheets, the arrangement is placed on the thermocouple such that the center of the mold is on the thermocouple. The top circular ring of the chamber is then positioned such that the magnets on the ring are placed in the grooves of the bottom ring. This ensures that the mold and the substrate are locked in their places with the thermocouple underneath them. This arrangement is shown in Figure 4.9.

After ensuring proper placement of the mold and the substrate on top of the thermocouple, the chamber is pushed inside the equipment and the whole arrangement is brought under vacuum to eliminate particle contamination. Pressure is applied uni-

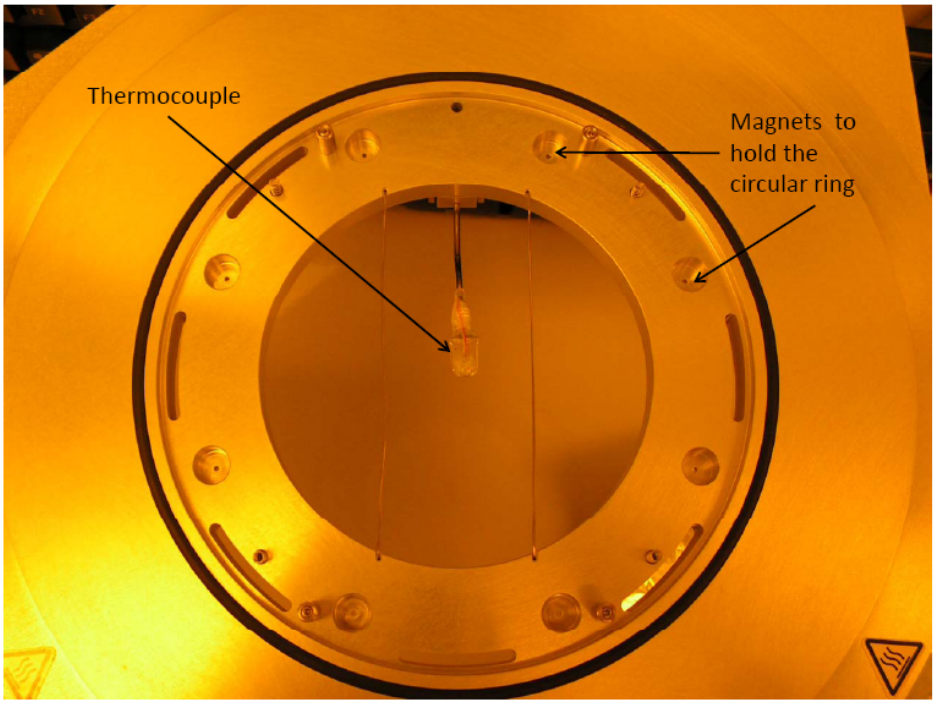

Figure 4.9. The chamber which houses the mold and wafer during imprinting.

formly on both the mold and the substrate to transfer pattern form the mold to the substrate. Temperature of the sample is kept constant with the use of thermocouple and heater. Once the imprinting is done, the temperature is lowered to room temperature and the pressure is lowered to atmospheric pressure. The substrate and the mold are taken out of the chamber and the mold is separated from the substrate.

4.6.1 Imprint results

The imprinting of the samples was done using the mold that was purchased from NIL technologies, Denmark. Figure 4.10 shows the SEM image of an imprinted sample with pores on the imprint resist. The pore diameter shown in the image is about 211 nm, within specification given by the company. Figure 4.11 shows an SEM image which is close to the cross-section of the imprinted sample. The height of the imprinted hole was found to be 97.72 nm and the thickness of the resist was found

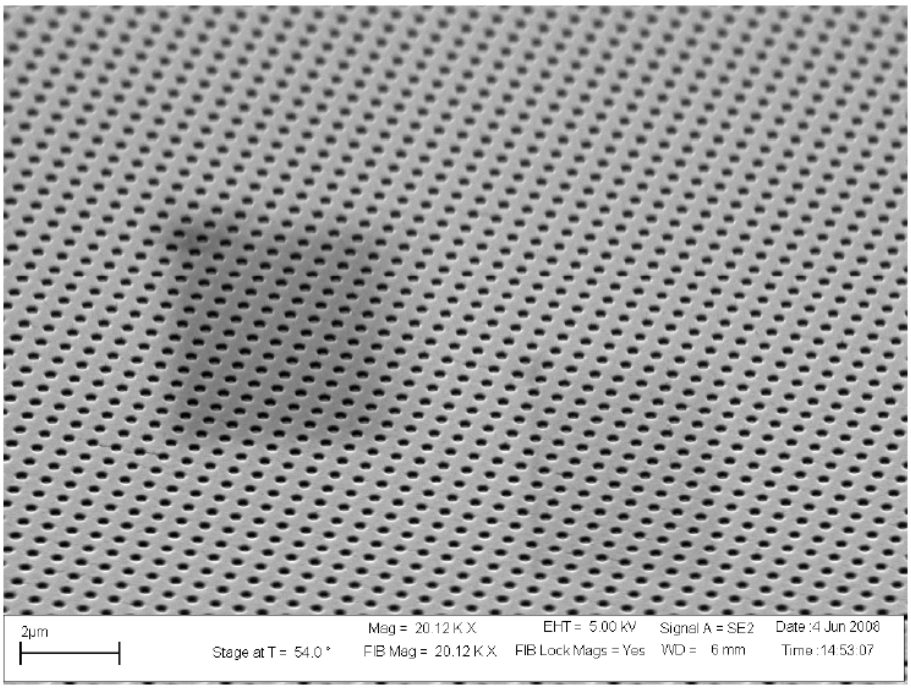

Figure 4.10. SEM image of imprint on resist. The pore dimension is 211 nm.

to be 181.5 nm at an angle of 50 ^{o}. The actual values for the resist thickness and the imprint depth can then be easily calculated to be 127 nm and 236 nm, respectively.

4.6.2 Pattern transfer

The pattern from the resist was transferred to the substrates using RIE. The residual resist after imprinting was ashed with oxygen plasma at 100 W power with 0.3 mBar pressure. The time for ashing depends on the thickness of the residual resist, which in turn depends on the initial thickness of the resist and the pillar height on the mold. The desired residual resist thickness is around 30 - 60 nm. This ensures proper pattern transfer, and protects the features on the mold during imprinting. The etch rate of the residual resist was found to be around 8 - 10 nm a minute.

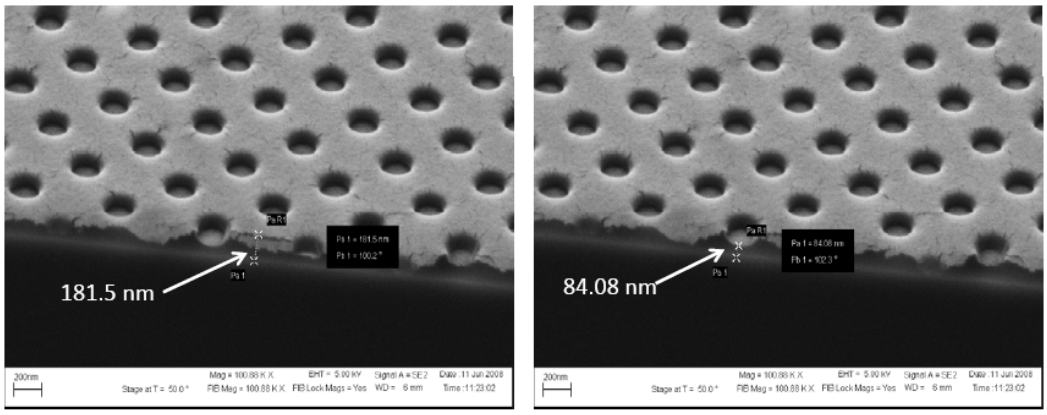

Figure 4.11. Cross-section of the imprinted resist.

The substrate was etched after ashing the resist using SF_6 (this process was done at UT Dallas). The power used for etching the substrate was 300 W and the pressure of the gas used was 20 SCCM. The etch rate of SI_3N_4 for this condition was determined to be 440 nm a minute. An image of the sample etched for 15 minutes is shown in Figure 4.12. From the image, it is evident that etching was not proper. This could be due to the following reasons

- The Inductive Coupled (ICP) power used in the system could be high. This is because of the fact that we used SF_6 gas to etch, which requires high power in the system to ignite and sustain the plasma. This could have caused eroding of the resist, which makes the mask for the substrate.
- The other reason for the improper etching could be due to the lateral etching of the resist, which could increase the pore dimension leading to pores merging.

One way to overcome these problems is by using CF_4 to etch the substrate, which requires less power to ignite and sustain plasma. This could reduce the attack on the resist during etching of the substrate

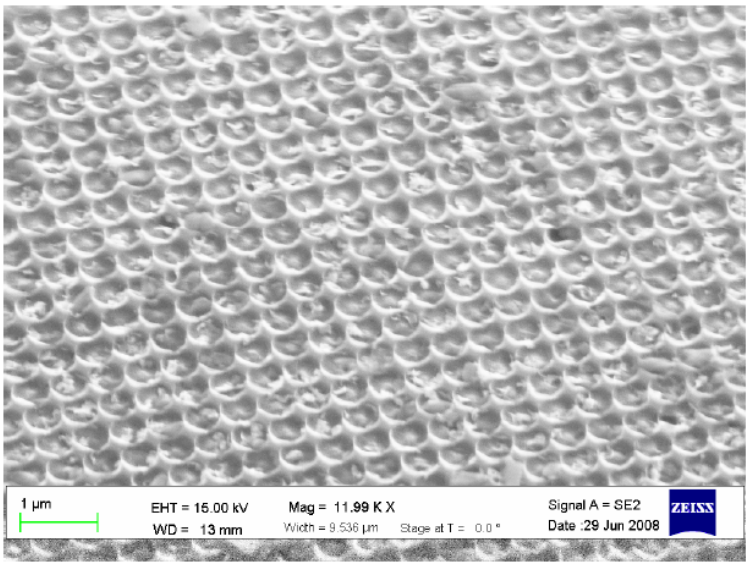

Figure 4.12. After etching the substrate for 15 minutes in SF_6 plasma.

4.7 Summary

This chapter briefly discussed the nanoimprint lithography (NIL) process and its applications. Different types of NIL were listed with focus on thermal imprint lithography. From the SEM images, the imprint was analyzed for uniformity and consistency of the imprint. The cross-section of the imprint was examined to determine the thickness of the residual resist. Finally, the process to etch the residual resist is also addressed.

CHAPTER 5

CONCLUSION

Porous membranes for blood oxygenation systems have been designed, simulated, and fabricated with different porosities and pore dimensions. Design and simulation was performed using Coventor Ware, software used in MEMS design and analysis. Different designs were utilized based on the number of gas channels per blood channel, blood channel dimensions, and gas channel dimensions. These designs were compared with each other based on the blood to gas volume ratio and the surface area of blood to gas interaction. Dome channel design and roof top dome channel design II were chosen for fabrication, since these designs had desirable blood to gas volume ratios of approximately 90%. The surface area of the interaction was 0.10 μm^{-1} for dome channel and was found to vary from 0.077 to 0.168 μm^{-1} for the roof-top dome channel II.

Low Pressure Chemical Vapor Deposition (LPCVD) silicon nitride was used as the membrane material due to its high Young's modulus of 304 GPa, and high yield strength. Potassium hydroxide was used as the wet etchant to remove Si, as KOH etches Si preferentially in the (100) plane when compared to the (111) plane.

Pores on the fabricated membranes were drilled initially using Focused Ion Beam (FIB). Membranes of different porosities and with different pore dimensions were fabricated, after which the porous membranes were tested for stability under pressure using a custom setup. The membranes were subjected to 50 times the pressure the membrane is expected to experience during normal operation. Results from the simulation and the practical experiments agreed at low pressures. At high pressures,

the simulation results and the experimental results deviated due to approximations in the calculations and assumptions in simulations. Ga^+ ions were the liquid metal ion source used in the FIB to drill pores on the membrane. FIB process is a sequential process and not a parallel process. This makes the process very time consuming which causes delay in fabrication.

Hence, a different fabrication technique was successfully used to fabricate pores on the membrane, eg. nanoimprinting. In this method, we employ a mold similar to the mask of optical photolithography to transfer pattern to the thermoplastic resist. The mold had pillars of diameter ranging from 150 nm to 250 nm, and the pitch was 500 nm. The resist, after the imprinting was ashed in oxygen plasma to remove the residual resist. The imprint from the resist was then transformed on to the silicon nitride underneath the resist using RIE. Silicon from the non-polished side of the wafer was etched to release the membrane.

Future work involves design and optimization of manifold for the inlet of deoxygenated blood, and the removal of oxygenated blood from the sample. In addition, biocompatible channels need to be fabricated for blood and gas flow towards the realization of implantable blood oxygenation system. They are both considerable tasks, but are reachable goals, according to current results and design plans.

APPENDIX A

FABRICATION OF SILICON NITRIDE MEMBRANES

In this appendix we describe the process flow for the fabrication of silicon nitride test membranes

1. The wafer is cleaned using the following cleaning process.
   (a) Rinse the wafer in TCE bath for 6 minutes.
   (b) Place the wafer in Methanol for 6 minutes.
   (c) Dip the wafer in Acetone bath for 6 minutes.
   (d) Rinse the wafer in DI water for 6 minutes.
   (e) Degrease the wafer in HCL: H2O2: H2O solution (mixture ratio is 1:2:7) for 3 minutes.
   (f) Rinse the wafer in DI water for 3 minutes.
   (g) Place the wafer in H2SO4:H2O2 solution for 3 minutes (Mixture ratio is 3:1)
   (h) Rinse the wafer in DI water for 3 minutes.
   (i) Repeat steps a-d.
   (j) Place the wafer in HF for a minute, rinse it in DI water, and blow-dry the wafer.
2. Deposit LPCVD silicon nitride on the cleaned wafer, to a thickness of approximately about 1 - 1.5 μm. The process flow for the deposition of LPCVD nitride is as follows
   (a) The furnace is heated to the required temperature of 835^oC. The wafers are loaded to the furnace slowly zone by zone so that no stress is induced on the wafer.
   (b) After carefully placing the wafers, the gases required for deposition is allowed to flow inside the furnace. The gases required for deposition are dichlorosilane (DCS) and ammonia. The flow rates of DCS is 20 sccm,

and ammonia is 100 sccm (sccm stands for standard cubic centimeter per minute, which is a unit of measurement of flow rate of gas).

(c) The pressure of the furnace is to be maintained at 250 mtorr.

The deposition rate of silicon nitride was found to be 2000 angstroms per hour. Silicon nitride was deposited for about 5 hours to obtain a 1 1-1.5 μm thick layer. The uniformity of the nitride varied to about 5% all through the wafer. (LPCVD nitride was deposited at UTD using their LPCVD furnace and process flow information given above is their standard low stress nitride process flow). Figure A.1 depicts the cross section of wafer after deposition of silicon nitride using LPCVD technique.

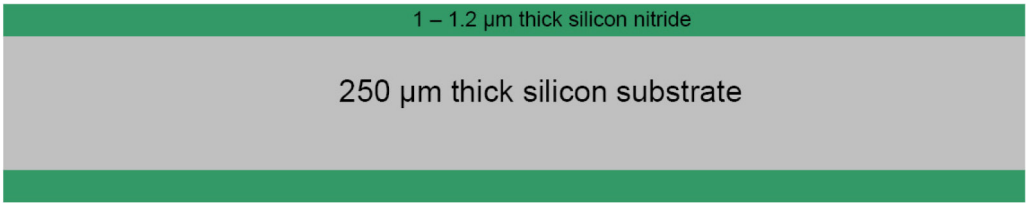

Figure A.1. Deposition of LPCVD Silicon Nitride.

3. After the deposition of low stress LPCVD silicon nitride, the wafer was patterned using SU-8 2010 photo resist. The process for patterning the silicon nitride using SU-8 2010 is described below:

   (a) The photoresist is deposited by spin-casting deposition technique, on the polished side of the wafer. Initially the spin speed is set at 500 rpm with a ramp of 100 rpm/sec for 5 sec, this is done to spread the resist. The spin speed is then increased to 1100 rpm with a ramp of 300 rpm/sec for 30 sec to obtain the desired thickness.

(b) The wafer is then baked at 65 ^oC for 1 min and then at 95 ^oC for 3 minutes for pre exposure bake.

(c) After, baking the wafer the photoresist is exposed to UV light for 7.7 seconds in OAI aligner.

(d) The exposed wafer is then baked at 65 ^oC for 1 min and then at 95 ^oC for 2 minutes. This step is known as post exposure bake. This is done to improve the resistance of the exposed regions to chemical treatment.

(e) The wafer is then developed for 3 minutes in SU-8 developer with constant agitation for every 10 seconds.

(f) After development, the wafer is heated at 140 ^oC for 1 minute. This is done to reflow the developed photoresist, which reduces cracks on the surface of photoresist.

After hard baked, the wafer is inspected under optical microscope. The pattern was checked for thickness of the photoresist in profilometer and the thickness of photoresist was found to be 19 - 21 μm. Figure A.2 shows the cross section of the wafer after patterning the wafer using SU-8 2010.

Figure A.2. Corss-section of wafer after Lithography.

4. The wafers with patterned SU-8 2010 are placed on a 4-inch wafer using silver paint. Silver paint is a colloidal solution of silver which is used to stick wafers

together in clean room environment. The recipe for etching nitride in DRIE is as given in Table A.1.

Parameter	**Value**
Chamber Pressure	750 mTorr
ICP Power	0 Watts
RIE Lower Chuck power	400 Watts
He (for clamp)	5 sccm
CF_4	25 sccm
He	25 sccm
SF_6	70 sccm
Ar	70 sccm

Table A.1. DRIE paramters for etching silicon nitride

Figure A.3. Cross-section of wafer after patterning the nitride using DRIE.

5. After etching silicon nitride in DRIE, the feature depth was checked using profilometer and was found to be 23 to 26 μm. This shows that the nitride in the patterned region is completely removed.
6. Once the nitride is removed, the silicon in the exposed regions is etched using KOH. The processing conditions for etching silicon in KOH is
   (a) 30% or 50 % KOH is prepared from flakes of KOH and DI water. The prepared solution was heated to 85 ^oC.

(b) The processed sample is placed in the heated KOH solution. Silicon in the exposed regions was etched at 0.7-1 μm/min in 50 % KOH solution and 1-1.4 μm/min in 30 % KOH solution. The etch rate of silicon was found to decrease with time as predicted in the theory.[Please refer to Chapter 1]

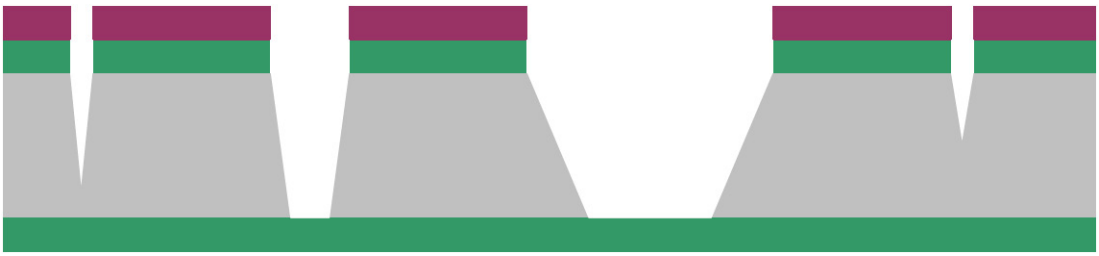

Figure A.4. Corss-section of wafer after etching silicon.

7. When the silicon is removed from the patterned regions, the etching automatically stops. Silicon nitride on the other side of the wafer acts as a etch stop, as silicon nitride is not etched by KOH. This is identified with the cessation of evolution of hydrogen from places where silicon was etched. SEM images of the membrane fabricated are shown in Figure 3.5 (Please refer to Chapter 3).

REFERENCES

[1] [Online]. Available: http://faculty.etsu.edu/currie/images/resp12.jpg

[2] [Online]. Available: http://cardiacsurgery.ctsnetbooks.org/cgi/content-nw/full/2/2003/317/F4

[3] J. J. Reilly, *Lung transplantation and Lung volume reduction surgery*. Cambridge, MA, 2004.

[4] R. Kotloff, "Lung transplantation," *New England journal of medicine*, vol. 350(11), pp. 1161–1162, 2004.

[5] B. G. High K, Sinder M, *"Gas exchange, heat transfer, and blood-artificial surface interactions" : Cardiopulmonary Bypass Principles and Practices*. Baltimore: Williams and Wilkins, 1993.

[6] R. F. D. Glenn P. Gravlee and J. R. Utley, *Cardiopulmonary Bypass: Principles and Practice*. Lippincott Williams and Wilkins, 1993.

[7] *Data for Spiral Coil Membrane Lung, Avecor Cardiovascular, formerly Sci-Med Life Systems*. Minneapolis, MN.

[8] A. C. Guyton and J. E. Hall, *Textbook of Medical Physiology 10th Edition*. Philadelphia: WB Saunders Co., 2000.

[9] C. J. C. Andreas O. Frank and R. L. Johnson, "A finite element model of oxygen diffusion in the pulmonary capillaries," *Journal of Applied Physiology*, vol. 82, no. 6, pp. 2036–2044, 1997.

[10] G. T.A.Kovacs, *Micromachined Transducers Sourcebook*. McGraw-Hill Series in Electrical and Computer Engineering, 1998.

[11] A. B. Lara Leoni and T. A. Desai, "Characterization of nanoporous membranes for immunoisolation : Diffusion properties and tissue effects," *Biomedical Microdevices*, vol. 4, no. 2, pp. 131–139, 2002.

[12] W. Venstra and P. Sarro, "Fabrication of crystalline membranes oriented in the (111) plane and in a (100) silicon wafer," *Microelectronic Engineering*, vol. 67-68, pp. 502–507, 2003.

[13] M. U. Jon Orloff and L. Swanson, *High resolution Focused Ion beams FIB and its applications*. Kluwer Academic/ Plenum Publishers, 2003.

[14] P. Prewett and G.L.R.Mair, *Focused Ion Beams from Liquid Metal Ion Sources*. Research Studies Press Ltd./ John Wiley and Sons Inc., 1991.

[15] Wikipedia. [Online]. Available: http://en.wikipedia.org/wiki/Lithography

[16] T. Nielsen, "Nanoimprint lithography," M.Sc Thesis, Technical University of Denmark, Denmark, 2003.

[17] C. M. S. Torres, *Alternative lithography Unleashing the potentials of Nanotechnology*. Kluwer Academic/ Plenum Publishers, 2003.

BIOGRAPHICAL STATEMENT

Vijayakrishnan Ambravaneswaran was born in Chennai, India, in 1983. He received his B.E. degree from Anna University, Chennai, India, in 2005. His current research interest includes MEMS sensors, BioMEMS devices for cell characterization, drug delivery, neural implants and implantable devices.